Modeling the flow-induced anisotropic effective viscosity of fiber suspensions by mean-field and full-field homogenization

Zur Erlangung des akademischen Grades eines

DOKTORS DER INGENIEURWISSENSCHAFTEN (Dr.-Ing.)

von der KIT-Fakultät für Maschinenbau des

Karlsruher Instituts für Technologie (KIT)

angenommene

DISSERTATION

von

M.Sc. Róbert Bertóti

Tag der mündlichen Prüfung:	19. Januar 2021
Hauptreferent:	Prof. Dr.-Ing. Thomas Böhlke
Korreferent:	Prof. Dr. Andrew N. Hrymak
Korreferent:	Jun.-Prof. Dr. rer. nat. Matti Schneider

To my students

Zusammenfassung

In der vorliegenden Arbeit wird die strömungsinduzierte Anisotropie von Fasersuspensionen modelliert. Die eingetauchten Fasern können sich aufgrund der Strömung umorientieren, und die momentane Faserorientierungsverteilung beeinflusst wiederum die Strömung.

Der erste Effekt, die Entwicklung der Faserorientierung, ist in der Literatur weitgehend untersucht und zahlreiche Modelle sind bereits in kommerziellen Softwarepaketen implementiert. In den meisten Modellen werden Faserorientierungstensoren verwendet, um die Anisotropie und die Entwicklung der Faserorientierungsverteilung zu beschreiben.

Für den zweiten Effekt, die Anisotropie der effektiven Viskosität, gibt es auch Modelle in der Literatur, aber diese werden meistens nicht in den Formfüllsimulationen berücksichtigt. Die Gründe für die Vernachlässigung sind die Anzahl, die komplexe Mikrostrukturabhängigkeit und die bisher fehlenden experimentellen Valdierung der Parameter. Ein weiterer Grund dafür, dass meistens nur isotrope effektive Viskositätsmodelle in Formfüllsimulationen verwendet werden ist numerische Instabilität, die bei der numerischen Berücksichtigung der Anisotropie der Viskosität auftritt.

Das wichtigste neue Ergebnis dieser Arbeit ist die Bewertung einer Mean-Field-Homogenisierungsmethode durch Vollfeldsimulationen, d.h. durch numerische Experimente, unter Berücksichtigung der anisotropen effektiven Viskosität von Fasersuspensionen.

Die allgemeine Form des effektiven, linearen Viskositätstensors wird unter Verwendung von drei Viskositätsparametern abgeleitet, wobei

von starren, geraden Fasern und einer inkompressiblen Flüssigkeit ausgegangen wird. Die Abhängigkeit der drei Viskositätsparameter von den Mikrostruktureigenschaften – dem Faservolumenanteil, dem Faserlängen-Durchmesser-Aspektverhältnis und der Flüssigkeitsviskosität – wird durch Mean-Field-Homogenisierung bestimmt.

Zusätzlich wird der effektive Viskositätstensor ebenfalls durch Vollfeld-Homogenisierung berechnet, basierend auf repräsentativen Volumenelementen synthetischer Mikrostrukturen, und die zugehörigen Viskositätsparameter werden numerisch bestimmt.

Die resultierenden Viskositätsparameter des Mean-Field- und des Vollfeld-Homogenisierungsverfahrens werden miteinander verglichen, und die Fehler in Bezug auf die numerisch berechneten effektiven Viskositätstensoren werden angegeben. Es wird beobachtet, dass die relativen Fehler im Falle der Bestimmung der Viskositätsparameter mittels der Vollfeldmodells etwa eine Größenordnung kleiner sind als die Fehler bei der Verwendung des Mean-Field-Modells. Zudem werden analytische Näherungen der Vollfeldviskositätsparametern angegeben, die zur Verwendung in Formfüllungssimulationen empfohlen werden.

Summary

In this work, the flow-induced anisotropy of fiber suspensions is modeled. The immersed fibers can reorientate themselves due to the flow, and on the other hand, the momentary fiber-orientation distribution influences the flow.

The first effect, i.e., the fiber-orientation evolution, is widely investigated in the literature, and various models are already implemented in commercial software packages. In most models, fiber-orientation tensors are used for describing the anisotropy and the evolution of the fiber-orientation distribution.

For the second effect, i.e., the anisotropy of the effective viscosity, models already exist in the literature, these are, however, usually not taken into account in form-filling simulations. The reasons for this neglect are the number, the complex microstructure dependence, and the lack of experimental validation of the parameters. Another reason for the fact that mostly only isotropic effective viscosity models are used in form-filling simulations is the numerical instability which occurs when the anisotropy of the viscosity is taken into account numerically.

The main novelty of this work is the evaluation of the accuracy of a mean-field homogenization method by full-field simulations, i.e., by numerical experiments, considering the anisotropic effective viscosity of fiber suspensions.

The general form of the effective linear viscosity tensor is derived with the use of three viscosity parameters, assuming rigid straight fibers and an incompressible fluid. The dependence of the three viscosity

parameters on the microstructure properties – which are the fiber volume fraction, the fiber length to diameter aspect ratio and the fluid viscosity – are determined through mean-field homogenization.

In addition, the effective viscosity tensor is computed by full-field homogenization, based on representative volume elements of synthetic microstructures, and the corresponding viscosity parameters are determined numerically.

The resulting viscosity parameters of the mean-field and the full-field homogenization methods are compared to each other, and the errors relative to the numerically computed effective viscosity tensors are determined. It is observed that the relative errors caused by the viscosity parameters of the full-field model are about one order of magnitude smaller than the errors of the mean-field model. Analytical approximations of the full-field viscosity parameters are derived, which are recommended to be used in form-filling simulations.

Acknowledgments

I would like to thank Professor Böhlke for supervising the thesis, for his introduction to the topics of anisotropy and homogenization, and for making my doctorate possible. I would like to thank him for his excellent teaching which motivated me to pursue my doctorate at ITM.

I would also like to thank Professor Hrymak for the co-supervision of my thesis, and the collaborative support during my research visit at the University of Western Ontario and at the Summer Schools of the IRTG 2078.

My special thanks go to Matti Schneider, his preliminary work and the software tools (voxelizerKIT and homKIT) developed by him are the basis of the numerical part of this work.

I would like to thank Daniel, Lore, Andi, Johannes, Mauricio, Peter, Ulrich, Fabian, my ITM colleagues and the IRTG 2078 PhD students for the numerous technical discussions. I thank Tom, Helga and Ute for all their organisational support.

The research documented in this doctoral thesis has been partially funded by the German Research Foundation (DFG) within the International Research Training Group "Integrated engineering of continuous-discontinuous long fiber reinforced polymer structures" (IRTG 2078). The support by the German Research Foundation (DFG) is gratefully acknowledged.

Karlsruhe, June 2020 Róbert Bertóti

Contents

Chapter 1

Introduction

1.1 Motivation

Reinforcing polymers with discontinuous fibers is a commonly used way to achieve higher stiffness, while keeping the high formability and low production costs of unfilled polymers, still using the commonly spread injection- or compression molding production technology.

During the molding process the discontinuous fibers continuously reorientate which causes steadily changing anisotropic effective viscosity. The reorientation of the fibers leads to an inhomogeneous final fiber orientation distribution and anisotropic effective material properties of the produced, solidified parts. The effective material anisotropy can be measured after production, with the help of different load cases and the deformation response. Another way to characterize the anisotropy of a part is to measure the fiber-orientation distribution, e.g., by computer tomography, and compute the effective anisotropic material properties with the help of homogenization methods. Both methods include costly – and mostly destructive – measurements, and expensive prototypes of the designed part have to be produced.

Knowledge about the evolution of the anisotropy during the production process gives the opportunity to have more control on the final anisotropy of the produced part. For this reason, in the case of injection- and compression molding, the anisotropy of fiber suspensions has to

be investigated, i.e., the anisotropy of the effective viscosity. As a first approximation, the material behavior can be modeled as linear viscous. Neglecting the non-linearity of the polymer melt is a simplification, but a reasonable one to better understand the flow process.

The numerical determination of the effective viscosity allows prediction of the anisotropic effective material behavior of a designed part, without measurements and costly production. Whether the predictions of the simulations – based on assumptions – are correct, has to be validated with some measurements but less of them is enough than without simulations.

Originality of the thesis. This work exhibits the following novelties:

- **Tensor form of the transversely isotropic effective viscosity, in the case of incompressibility:** A transversely isotropic tensor of fourth order, like the effective viscosity tensor in the case of aligned fibers, has in general five independent coefficients. In the case of incompressibility the number of the independent coefficients reduces to three. In several papers the second-order tensor equation of the deviatoric stress–deviatoric strain rate relation, as function of the tree viscosity coefficients and the fiber-orientation tensors, is stated, e.g., Tucker III (1991). In this work the fourth-order tensor of the effective viscosity is reparameterized as function of the three viscosity coefficients and the fiber-orientation tensors which is a more general description.
- **Determining the viscosity coefficients by mean-field homogenization:** The three viscosity coefficients are determined using the Mori-Tanaka method, for the special case of incompressible matrix and rigid fibers. The applied Eshelby's tensor is singular due to the considered special case and it has to be inverted on the non-singular subspace. The considered microstructure parameters are the matrix viscosity, the fiber volume fraction and the fiber aspect ratio.

- **Computing the viscosity tensor through full-field homogenization:** The viscosity tensor is computed by FFT-based full-field homogenization, with the use of synthetic microstructures. The orientation space is parameterized with the second-order fiber orientation tensor. The three vertexes of the fiber-orientation triangle, i.e., unidirectional, planar isotropic and isotropic orientation cases are investigated. The size of the representative volume element is investigated in each case. The independence of the approximated viscosity coefficients on the fiber-orientation state is investigated.
- **Improving the analytical predictions of the mean-field model based on the numerical results of the full-field simulations:** Improved analytical forms of the viscosity coefficients are recommended, based on the numerical results of the full-field computations, for the investigated microstructure parameter range.

1.2 State of the art

Flow-induced anisotropy of the fiber orientation. The reorientation of a single fiber in an incompressible isotropic Newtonian fluid was first described by Jeffery (1922). This is the basis of all later fiber evolution models which are widely used today in form-filling softwares. A more general derivation of Jeffery's equation is given by Junk and Illner (2007).

To describe the orientation state and the dynamics of rigid fiber systems – in a numerically efficient way – Advani and Tucker III (1987) introduced the fiber-orientation tensors of the first kind (Kanatani, 1984). These tensors are used – similarly as the texture coefficients for polycrystals (Böhlke and Bertram, 2001; Böhlke et al., 2003; Böhlke, 2006) – to describe the anisotropy evolution caused by the deformation process.

Jeffery's equation, also in the tensorial form, accounts only for the effect of the hydrodynamic forces, but does not include the fiber-fiber interaction which plays an important role for higher fiber volume fractions. For many fiber systems the fiber-fiber interactions are modeled with the use of phenomenological interaction coefficients. The most often used models are the Folgar-Tucker (Folgar and Tucker III, 1984), the Reduced Strain Closure (Wang et al., 2008) and the Anisotropic Rotary Diffusion (Phelps and Tucker III, 2009). The interaction coefficients can be determined empirically, see for example the works presented by Bay and Tucker III (1992a;b) and Phan-Thien et al. (2002). Slightly modified versions of these theories are given by the Retarding Principal Rate model (Tseng et al., 2013b) and the objective improved Anisotropic Rotary Diffusion model (Tseng et al., 2013a; 2016). All of these models and their combinations are nowadays implemented in open source and commercial software packages, see some applications presented by Tang and Altan (1995); Chung and Kwon (2002b); Ospald (2014) and Bertóti and Böhlke (2017a).

The extensions of Jeffery's equation in the tensorial form need a closure application to approximate the arising fourth-order fiber-orientation tensor, see for example the papers presented by Doi (1981); Hand (1962); Advani and Tucker III (1990); Verleye (1993); Cintra Jr and Tucker III (1995) and Chung and Kwon (2002a). For special cases there also exist closure-free models, see (Montgomery-Smith et al., 2011a) and (Montgomery-Smith et al., 2011b).

The above mentioned models consider how the fluid flow affects the fiber reorientation but they neglect the back-coupling, namely the effect of the permanently changing fiber orientation on the fluid flow. In the next paragraph the models considering the back-coupling are summarized.

Effective-viscosity models for fiber reinforced polymer melts. The rheology of fiber suspensions is described by various models in the literature. If a molten composite is considered to be linear and isotropic, then the viscosity model of Newtonian fluids (Newton, 1999) is applicable, by describing the fiber-matrix mixture with an effective scalar viscosity, which can be measured by a shear rheometer (Eschbach, 1993).

But polymer melts show a strongly nonlinear behaviour, see for example (Ferry, 1980). The stress is not directly proportional to the strain rate, even not for pure molten polymers, this is the so-called shear-thinning behaviour, often described by the Cross-model (Cross, 1970). Considering filled polymer melts, the nonlinear stress–strain rate relation is described, e.g., by Poslinski et al. (1988).

In the case of polymer melts the temperature dependence of the viscosity is also notable, which is commonly described by the WLF model (Williams et al., 1955).

Nowadays, in commercial software, for modeling the flow of fiber reinforced polymer melts, nonlinear behaviors are included, i.e., shear thinning behaviour, and the temperature dependence of the fiber-fluid mixture is implemented, see for example (Koszkul and Nabialek, 2004).

In contrast, the anisotropy of the suspensions is not accounted for in most of the simulations/simulation codes.

The anisotropy of fiber suspensions, e.g., glass fibers immersed in a polymer matrix, is similar to the anisotropy of liquid crystals (Oseen, 1933; Papenfuss and Muschik, 2018) but due to the long range interaction of the fibers their descriptions are not identical to liquid crystals (Ericksen, 1959; 1960a).

One of the first constitutive laws considering the anisotropic flow properties of fiber suspensions is the Transversely Isotropic Fluid (TIF) model from Ericksen (1960b). The models by Hinch and Leal (1972); Brenner (1974); Dinh and Armstrong (1984); Lipscomb II et al. (1988); Pipes et al. (1991) and Phan-Thien and Graham (1991) are modifications of the TIF model and they all depend linearly on the fourth-order fiber-orientation tensor, similarly as the models presented in (Bertóti and Böhlke, 2016; 2017b; Bertóti et al., 2020a;b) and in this work.

Numerical implementations of the above mentioned models are presented by Alexandrou and Mitsoulis (2007); Heinen (2007); Latz et al. (2010); Bertóti and Böhlke (2017a); Sommer et al. (2018); Wittemann et al. (2019); Mezi et al. (2019) and Tseng and Favaloro (2019).

1.3 Notation, frequently used abbreviations and symbols

A direct tensor notation is preferred throughout the text. The tensor components are given with the use of Latin indices. Einstein's summation convention is applied. Three-dimensional space is considered. A Cartesian coordinate system is used. In the following, frequently used symbols, operators and abbreviations are listed. SI units are used, where nothing else is given.

Abbreviations

ap	Approximated
disc	Discrete model
fit	Fitted
iso	Isotropic orientation state, $\bar{\boldsymbol{N}}_{\text{iso}} \hat{=} \text{diag}(0.33, 0.33, 0.33)$
mf	Mean-field
num	Numerical
piso	Planar isotropic orientation state, $\bar{\boldsymbol{N}}_{\text{piso}} \hat{=} \text{diag}(0.5, 0.5, 0)$
quad	Quadratic closure
sf	Single fiber
ud	Unidirectional orientation state, $\bar{\boldsymbol{N}}_{\text{ud}} \hat{=} \text{diag}(1, 0, 0)$
FFT	Fast Fourier transformation
IBOF	Invariant-based optimal fitting
MT	Mori-Tanaka
RVE	Representative volume element
7715	Frequently formed orientation state, $\bar{\boldsymbol{N}}_{7715} \hat{=} \text{diag}(0.77, 0.15, 0)$

Greek letters

α	Serial number
β_i	Scalar coefficients
$\bar{\varepsilon}_{\text{M}}$	Effective von Mises equivalent strain
η	Shear viscosity
$\bar{\eta}$	Effective viscosity
$\bar{\eta}_{\text{s}}$	Effective shear viscosity
$\bar{\eta}_{\text{v}}$	Effective volume viscosity
λ_1	First largest eigenvalue of $\bar{\boldsymbol{N}}$
λ_2	Second largest eigenvalue of $\bar{\boldsymbol{N}}$
$\bar{\nu}$	Effective Poisson's ratio
ξ	Geometry parameter of a fiber
$\bar{\boldsymbol{\sigma}}$	Effective Cauchy stress tensor

Latin letters

$\bar{c}_\mathrm{f}$	Fiber volume fraction
d	Diameter of a fiber
e	Error
l	Length of a fiber
r_a	Aspect ratio of a fiber
t	Time
Δt	Time step
$\bar{K}$	Effective bulk modulus
L	Length of a volume element
M	Total number of fibers
$\bar{N}_\mathrm{s}$	Shear number
$\bar{N}_\mathrm{p}$	Particle number
P	Permutation symbol
W	Width of a volume element
$\boldsymbol{n}$	Fiber-orientation vector
$\bar{\boldsymbol{v}}$	Effective velocity vector
$\boldsymbol{x}$	Position vector
$\bar{\boldsymbol{D}}$	Effective strain rate tensor
$\bar{\boldsymbol{L}}$	Effective velocity gradient
$\bar{\boldsymbol{N}}$	Fiber-orientation tensor of second order
$\boldsymbol{P}$	Eigenprojector
$\bar{\boldsymbol{W}}$	Effective vorticity tensor
$\mathbf{1}$	Second-order identity tensor
$\mathbb{E}$	Eshelby tensor
$\mathbb{I}$	Fourth-order identity tensor
$\mathbb{I}^\mathsf{s}$	Right-symmetric part of the fourth-order identity tensor
$\bar{\mathbb{N}}$	Fiber-orientation tensor of fourth order
$\mathbb{P}_1$	First projector tensor of fourth order: $\mathbb{P}_1 = \mathbf{1} \otimes \mathbf{1}/3$
$\mathbb{P}_2$	Second projector tensor of fourth order: $\mathbb{P}_1 = \mathbb{I}^\mathsf{s} - \mathbb{P}_1$
$\bar{\mathbb{V}}$	Effective viscosity tensor

Operators

$\boldsymbol{A} \cdot \boldsymbol{B}$	Scalar product : $\boldsymbol{A} \cdot \boldsymbol{B}{=}A_{ij}B_{ij}$
$\|\|\boldsymbol{A}\|\|$	Frobenius norm: $\|\|\boldsymbol{A}\|\| = \sqrt{\boldsymbol{A} \cdot \boldsymbol{A}}$
$\boldsymbol{A} \otimes \boldsymbol{B}$	Dyadic product: $(\boldsymbol{A} \otimes \boldsymbol{B})_{ijkl}{=}A_{ij}B_{kl}$
$\mathrm{tr}(\boldsymbol{A})$	Trace of a second-order tensor: $\mathrm{tr}(\boldsymbol{A}){=}\boldsymbol{A} \cdot \boldsymbol{1}{=}A_{ii}$
$\boldsymbol{AB}$	Composition of second-order tensors: $(\boldsymbol{AB})_{ij}{=}A_{ik}B_{kj}$
$\mathbb{A}[\boldsymbol{B}]$	Linear mapping of a second-order tensor by a fourth-order tensor: $(\mathbb{A}[\boldsymbol{B}])_{ij}{=}A_{ijkl}B_{kl}$
$\boldsymbol{A}\square\boldsymbol{B}$	Box product of second-order tensors: $(\boldsymbol{A}\square\boldsymbol{B})_{ijkl}{=}A_{ik}B_{lj}$
$\mathbb{A}^{\mathsf{T_R}}$	Right minor transposition: $(\mathbb{A}^{\mathsf{T_R}})_{ijkl}{=}A_{ijlk}$
$\mathbb{A} : \mathbb{B}$	Composition of fourth-order tensors: $(\mathbb{A} : \mathbb{B})_{ijkl}{=}A_{ijmn}B_{mnkl}$
$\mathrm{S}(\mathbb{A})$	Fully symmetrization of a fourth-order tensor: $\mathrm{S}(A_{ijkl}){=}1/24 \sum_{\alpha=1}^{24} A_{P_\alpha(i,j,k,l)}$

Subscripts and superscripts

$\bar{(\cdot)}$	Effective, macroscopic value
$(\cdot)'$	Deviatoric part
$\dot{(\cdot)}$	Material time derivative
$(\cdot)_{\mathrm{f}}$	Property belonging to the fiber
$(\cdot)_{\mathrm{m}}$	Property belonging to the matrix
$(\cdot)^{\mathrm{cf}}$	Property belonging to the compressional flow
$(\cdot)^{\mathrm{aniso}}$	Anisotropic part of a tensor
$(\cdot)^{\mathrm{ef}}$	Property belonging to the elongational flow
$(\cdot)^{\mathrm{iso}}$	Isotropic part of a tensor
$(\cdot)^{\mathrm{pf}}$	Property belonging to the planar flow
$(\cdot)^{\mathrm{sf}}$	Property belonging to the shear flow

Chapter 2

Modeling preliminaries

2.1 Assumptions on incompressible short-fiber suspensions

2.1.1 Microstructure of short-fiber suspensions

Straight, cylindrical, rigid fibers with the length l and diameter d, immersed in an incompressible Newtonian fluid are considered in this work. The modeled microstucture parameters are: the fiber aspect ratio $r_\mathrm{a} = l/d$ which is considered to be constant, the fiber volume fraction $\bar{c}_\mathrm{f}$, the isotropic scalar viscosity of the surrounding fluid referred as matrix viscosity η_m, and the fiber-orientation distribution described by the normalized vectors $\boldsymbol{n}_\alpha$, where $\alpha = 1, \ldots, M$ is the index corresponding to each of the fibers. The rigid fibers are modeled by infinite isotropic scalar viscosity $\eta_\mathrm{f} = \infty$. The possible shear-thinning behavior and the temperature dependence of the matrix viscosity η_m are neglected in this work.

The orientation distribution of fiber systems is exactly described by the fiber-orientation distribution function $f(\boldsymbol{n})$ which is defined on the surface of a unit sphere $S = \{\boldsymbol{n} \in \mathbb{R}^3 : ||\boldsymbol{n}|| = 1\}$. The function $f(\boldsymbol{n})$ is non-negative, centrosymmetric and normalized

$$f(\boldsymbol{n}) \geq 0, \quad f(-\boldsymbol{n}) = f(\boldsymbol{n}), \quad \int_S f(\boldsymbol{n}) \, \mathrm{d}S = 1, \tag{2.1}$$

where the surface element $\mathrm{d}S = \sin\vartheta/(4\pi)\,\mathrm{d}\varphi\,\mathrm{d}\vartheta$ with the azimuthal and polar angles φ and ϑ, respectively. The empirical orientation distribution function of M equally weighted fiber orientations $\boldsymbol{n}_\alpha$ is defined by

$$f(\boldsymbol{n}) = \frac{1}{2M}\sum_{\alpha=1}^{M}\left(\delta(\boldsymbol{n},\boldsymbol{n}_\alpha) + \delta(-\boldsymbol{n},\boldsymbol{n}_\alpha)\right), \tag{2.2}$$

utilizing Dirac's delta distribution function $\delta(\boldsymbol{n},\boldsymbol{n}_\alpha)$. The fiber-orientation distribution is approximately described by the fiber-orientation tensors of second- and fourth order (Advani and Tucker III, 1987), denoted by $\bar{\boldsymbol{N}}$ and $\bar{\mathbb{N}}$, respectively, and defined by

$$\bar{\boldsymbol{N}} = \int_S \boldsymbol{n}\otimes\boldsymbol{n}\, f(\boldsymbol{n})\,\mathrm{d}S, \quad \bar{\mathbb{N}} = \int_S \boldsymbol{n}\otimes\boldsymbol{n}\otimes\boldsymbol{n}\otimes\boldsymbol{n}\, f(\boldsymbol{n})\,\mathrm{d}S. \tag{2.3}$$

With the use of the empirical orientation distribution function

$$\bar{\boldsymbol{N}} = \frac{1}{M}\sum_{\alpha=1}^{M}\boldsymbol{n}_\alpha\otimes\boldsymbol{n}_\alpha, \quad \bar{\mathbb{N}} = \frac{1}{M}\sum_{\alpha=1}^{M}\boldsymbol{n}_\alpha\otimes\boldsymbol{n}_\alpha\otimes\boldsymbol{n}_\alpha\otimes\boldsymbol{n}_\alpha. \tag{2.4}$$

These fiber-orientation tensors are fabric tensors of the first kind (Kanatani, 1984), and they are used in the second step of the mean-field homogenization (see section 2.2 considering orientation averaging) and also as target value for the synthetic microstructure generation (see section 5.1.1). These orientation tensors of the first kind have all symmetries, i.e., symmetries for changing any two of their indexes, due to their definition (2.4). The reduction $\bar{\mathbb{N}}[\mathbf{1}] = \bar{\boldsymbol{N}}$ lowers the rank, and $\bar{\boldsymbol{N}}\cdot\mathbf{1} = 1$.

The two largest of the three eigenvalues of the second-order fiber-orientation tensor $\bar{\boldsymbol{N}}$ are denoted by λ_1 and λ_2, where $\lambda_1 \geq \lambda_2$. Considering the two largest eigenvalues of $\bar{\boldsymbol{N}}$, the orientation space reduces to a planar triangle, shown in Figure 2.1, similarly colored as in Köbler et al. (2018). The reduced fiber-orientation triangle describes

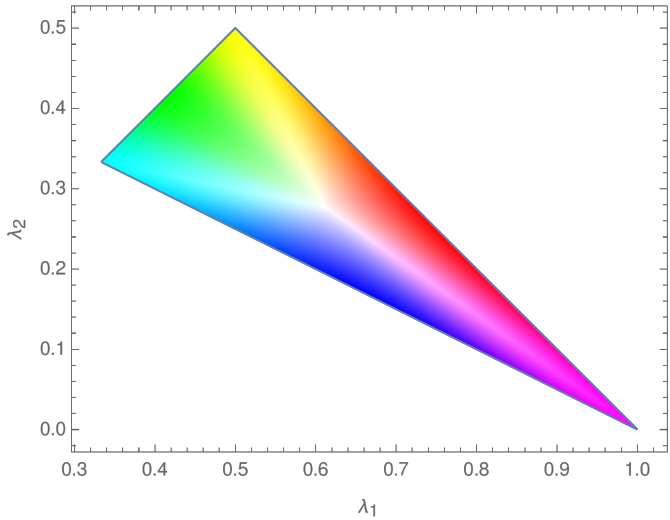

Figure 2.1: Fiber-orientation reference triangle, where $\lambda_1 \geq \lambda_2$ are the two largest eigenvalues of the second-order fiber-orientation tensor $\bar{\boldsymbol{N}}$. The three extreme orientations are the isotropic $\lambda_1 = \lambda_2 = 1/3$ (cyan), the unidirectional $\lambda_1 = 1$ (magenta), and the planar isotropic $\lambda_1 = \lambda_2 = 1/2$ (yellow) cases. The colors of the intermediate orientations are the combinations of CMY, such that the middle of the triangle is white. (Köbler et al., 2018)

the second-order fiber-orientation tensor $\bar{\boldsymbol{N}}$ explicitly up to a rotation $\boldsymbol{R}$, i.e.,

$$\bar{\boldsymbol{N}} = \boldsymbol{R}\bar{\boldsymbol{\Lambda}}\boldsymbol{R}, \qquad \bar{\boldsymbol{\Lambda}} = \lambda_i \boldsymbol{P}_i^{\Lambda},$$
$$\lambda_1 \geq \lambda_2 \geq \lambda_3 \geq 0, \qquad \lambda_1 + \lambda_2 + \lambda_3 = 1.$$

The reduced orientation space and the color scheme of Figure 2.1 are used throughout sections 5.3 and 6.3.

Note that the fiber-orientation tensors of the first kind $\bar{\boldsymbol{N}}$ and $\bar{\mathbb{N}}$ do not contain all the information about $f(\boldsymbol{n})$ and that $\bar{\boldsymbol{N}}$ and $\bar{\mathbb{N}}$ are not independent ($\bar{\mathbb{N}}[\mathbf{1}] = \bar{\boldsymbol{N}}$). The orientation tensors of the second kind $\bar{\boldsymbol{G}}$

and $\bar{\mathbb{G}}$ minimize the approximation measure

$$E = \int_S \left(\bar{\boldsymbol{G}} \cdot \boldsymbol{n} \otimes \boldsymbol{n} + \bar{\mathbb{G}} \cdot \boldsymbol{n} \otimes \boldsymbol{n} \otimes \boldsymbol{n} \otimes \boldsymbol{n} - f(\boldsymbol{n})\right)^2 \mathrm{d}S \to \min \qquad (2.5)$$

of the exact orientation distribution function $f(\boldsymbol{n})$. The orientation tensors of the third kind $\bar{\boldsymbol{H}}$ and $\bar{\mathbb{H}}$ have the advantage that they are independent form each other. For the detailed derivation, special properties and explicit forms of the orientation tensors of the second and third kind, the reader is referred to Kanatani (1984).

2.1.2 Flow regimes

Three flow regimes of fiber suspensions are distinguished (Chung and Kwon, 2002a):

- *dilute* ($\bar{c}_\mathrm{f} \ll 1/r_\mathrm{a}^2$),
- *semi-dilute* ($1/r_\mathrm{a}^2 \ll \bar{c}_\mathrm{f} \ll 1/r_\mathrm{a}$) and
- *concentrated* ($\bar{c}_\mathrm{f} \gg 1/r_\mathrm{a}$).

The dimensionless measures $\bar{c}_\mathrm{f}\, r_\mathrm{a}^2$ and $\bar{c}_\mathrm{f}\, r_\mathrm{a}$ correspond to the number of interacting fibers, and the number of – one fiber diameter thick – layers which can be densely filled with the fibers within a cubic volume swept by a single fiber, respectively. It means that already for a small aspect ratio of $r_\mathrm{a} = 10$, the semi-dilute regime ends at fiber volume fractions much smaller than $1/r_\mathrm{a} = 10\%$. In the case of industrial applications, short fibers typically have an aspect ratio between 30 and 300 ($1/r_\mathrm{a} \approx 0.3\% - 3\%$). Thus, real manufacturing processes typically concerned with concentrated suspensions. The value of $\bar{c}_\mathrm{f}\, r_\mathrm{a}$ is typically in the range of 1 to 5 (Chung and Kwon, 2002a). Due to the lack of theoretical predictions, often dilute or semi-dilute models are used also in industrial cases. Also in this work, the models are derived under the (semi-)dilute assumption. Whether the models continue to be valid for higher concentration must be investigated later. There exist other

classifications of the flow regimes, e.g., by Tucker III (1991), where the classification is based on a narrow gap, which can be important if the fiber length to part thickness ratio is approximately one or higher.

2.1.3 Linear effective viscosity tensor in incompressible fiber suspensions

It is assumed that the fluid-fiber suspension is incompressible. The effective, i.e., macroscopic, Cauchy stress $\bar{\boldsymbol{\sigma}}$ is additively decomposed into a pressure-dependent spherical $-\bar{p}\,\mathbf{1}$ and a pressure-independent deviatoric $\bar{\boldsymbol{\sigma}}'$ part

$$\bar{\boldsymbol{\sigma}} = -\bar{p}\,\mathbf{1} + \bar{\boldsymbol{\sigma}}'. \tag{2.6}$$

In this work, only the pressure-independent deviatoric part of the Cauchy stress $\bar{\boldsymbol{\sigma}}$ is considered. Because of the assumed incompressibility, $\bar{p}$ is a reaction force determined by the boundary conditions.

It is also assumed that the effective viscous material behaviour is linear

$$\bar{\boldsymbol{\sigma}} = \bar{\mathbb{V}}[\bar{\boldsymbol{D}}], \qquad \bar{\boldsymbol{D}} = \bar{\mathbb{F}}[\bar{\boldsymbol{\sigma}}], \tag{2.7}$$

where $\bar{\boldsymbol{\sigma}}$ is the effective Cauchy stress, $\bar{\mathbb{V}}$ is the effective viscosity tensor, $\bar{\boldsymbol{D}}$ is the effective strain rate (i.e., the symmetric part of the velocity gradient) and $\bar{\mathbb{F}} = \bar{\mathbb{V}}^{-1}$ is the effective fluidity tensor. For the isotropic case

$$\bar{\mathbb{V}}_{\text{iso}} = 3\bar{\eta}_{\text{v}}\mathbb{P}_1^I + 2\bar{\eta}_{\text{s}}\mathbb{P}_2^I, \qquad \bar{\mathbb{F}}_{\text{iso}} = \bar{\mathbb{V}}_{\text{iso}}^{-1} = \frac{1}{3\bar{\eta}_{\text{v}}}\mathbb{P}_1^I + \frac{1}{2\bar{\eta}_{\text{s}}}\mathbb{P}_2^I, \tag{2.8}$$

where $\bar{\eta}_{\text{v}}$ is the effective volume viscosity and $\bar{\eta}_{\text{s}}$ the effective shear viscosity, $\mathbb{P}_1^I = \frac{1}{3}\mathbf{1} \otimes \mathbf{1}$ and $\mathbb{P}_2^I = \mathbb{I}^{\text{s}} - \mathbb{P}_1^I$ are the first and the second projector tensors with major and minor symmetry, $\mathbf{1}$ is the second-order

identity tensor, and $\mathbb{I}^{\mathsf{s}} = 1/2\,(\mathbb{I} + \mathbb{I}^{\mathsf{T_R}})$ is the right-symmetric part of the fourth-order identity tensor $\mathbb{I} = \mathbf{1}\square\mathbf{1}$.

For the incompressible purely viscous case $\bar{\eta}_{\mathrm{v}} \to \infty$, similarly to $\bar{K} \to \infty$ and $\bar{\nu} \to 0.5$ in the case of linear elasticity, where $\bar{K}$ and $\bar{\nu}$ are the effective bulk modulus and the effective Poisson's ratio, respectively. In the case of incompressibility only the deviatoric effective Cauchy stress $\bar{\boldsymbol{\sigma}}'$ is of principal interest

$$\bar{\boldsymbol{\sigma}}' = \bar{\mathbb{V}}'[\bar{\boldsymbol{D}}'], \qquad \bar{\boldsymbol{D}}' = \bar{\mathbb{F}}'[\bar{\boldsymbol{\sigma}}'], \tag{2.9}$$

where $\bar{\boldsymbol{\sigma}}' = \mathbb{P}_2^I[\bar{\boldsymbol{\sigma}}]$, $\bar{\mathbb{V}}' = \mathbb{P}_2^I : \bar{\mathbb{V}} : \mathbb{P}_2^I$, $\bar{\boldsymbol{D}}' = \mathbb{P}_2^I[\bar{\boldsymbol{D}}]$ and $\bar{\mathbb{F}}' = \mathbb{P}_2^I : \bar{\mathbb{F}} : \mathbb{P}_2^I$. In the isotropic case they have the form

$$\bar{\mathbb{V}}'_{\mathrm{iso}} = 2\bar{\eta}_{\mathrm{s}}\mathbb{P}_2^I \quad \text{and} \quad \bar{\mathbb{F}}'_{\mathrm{iso}} = \frac{1}{2\bar{\eta}_{\mathrm{s}}}\mathbb{P}_2^I. \tag{2.10}$$

Note that the effective viscosity $\bar{\mathbb{V}}'$ is only pseudo-invertible, because of the assumed incompressibility, i.e., invertible only on the non-singular subspace. The fluidity $\bar{\mathbb{F}}$ is used in the numerical computations (Schneider, 2016).

Simplification of the notation. The prime $'$ from $\bar{\mathbb{V}}'$ and the superscript ^{I} from $\mathbb{P}_1^I$ and $\mathbb{P}_2^I$ are dropped, as in this work only the incompressible case is considered and because the general projectors $\mathbb{P}_\alpha$ (Halmos, 1958) are not used here. So in the following $\bar{\mathbb{V}} = \bar{\mathbb{V}}'$, $\mathbb{P}_1 = \mathbb{P}_1^I$ and $\mathbb{P}_2 = \mathbb{P}_2^I$.

2.2 Viscosity parameters

A possible way to estimate the effective viscosity tensor is to apply a two-step homogenization theory, also known as orientation averaging technique (Advani and Tucker III, 1987) or as averaging over unidirectional pseudo-grains (Kammoun et al., 2011). In the first step, the effective

properties of an unidirectional (transversely isotropic) pseudo-grain are specified, and in the second step the differently oriented pseudo-grains are averaged. Considering the first step in the case of incompressibility and fibers pointing in the direction of the unit vector $\boldsymbol{n}$, the unidirectional effective viscosity tensor $\bar{\mathbb{V}}_{\mathrm{ud}}$ is transversely isotropic. Therefore, it has the form

$$\begin{aligned}\bar{\mathbb{V}}_{\mathrm{ud}}(\bar{\eta},\bar{N}_{\mathrm{s}},\bar{N}_{\mathrm{p}},\boldsymbol{n}) = 2\bar{\eta}\Bigg(&\mathbb{P}_2\\ &+\bar{N}_{\mathrm{s}}\left(\boldsymbol{n}\otimes\boldsymbol{n}\,\square\,\mathbf{1}+\mathbf{1}\,\square\,\boldsymbol{n}\otimes\boldsymbol{n}-\frac{2}{3}\left(\mathbf{1}\otimes\boldsymbol{n}\otimes\boldsymbol{n}+\boldsymbol{n}\otimes\boldsymbol{n}\otimes\mathbf{1}\right)+\frac{2}{3}\mathbb{P}_1\right)\\ &+\bar{N}_{\mathrm{p}}\left(\boldsymbol{n}\otimes\boldsymbol{n}\otimes\boldsymbol{n}\otimes\boldsymbol{n}-\frac{1}{3}\left(\mathbf{1}\otimes\boldsymbol{n}\otimes\boldsymbol{n}+\boldsymbol{n}\otimes\boldsymbol{n}\otimes\mathbf{1}\right)+\frac{1}{3}\mathbb{P}_1\right)\Bigg),\end{aligned} \tag{2.11}$$

derived based on the works Tucker III (1991); Fiolka (2008); Weise and Meyer (2010). The three scalar parameters $\bar{\eta},\bar{N}_{\mathrm{s}},\bar{N}_{\mathrm{p}}$ are the effective scalar viscosity, the shear number and the particle number, respectively, and they are referred in the succeeding as viscosity parameters.

Assuming that the three viscosity parameters are independent of the fiber-orientation state and by using orientation averaging (Advani and Tucker III, 1987), the viscosity tensor $\bar{\mathbb{V}}$ may be written in the form

$$\begin{aligned}\bar{\mathbb{V}}(\bar{\eta},\bar{N}_{\mathrm{s}},\bar{N}_{\mathrm{p}},\bar{\mathbb{N}}) = 2\bar{\eta}\Bigg(&\mathbb{P}_2\\ &+\bar{N}_{\mathrm{s}}\left(\bar{\boldsymbol{N}}\,\square\,\mathbf{1}+\mathbf{1}\,\square\,\bar{\boldsymbol{N}}-\frac{2}{3}\left(\mathbf{1}\otimes\bar{\boldsymbol{N}}+\bar{\boldsymbol{N}}\otimes\mathbf{1}\right)+\frac{2}{9}\left(\mathbf{1}\otimes\mathbf{1}\right)\right)\\ &+\bar{N}_{\mathrm{p}}\left(\bar{\mathbb{N}}-\frac{1}{3}\left(\mathbf{1}\otimes\bar{\boldsymbol{N}}+\bar{\boldsymbol{N}}\otimes\mathbf{1}\right)+\frac{1}{9}\left(\mathbf{1}\otimes\mathbf{1}\right)\right)\Bigg),\end{aligned} \tag{2.12}$$

considering arbitrary fiber-orientation distributions, described by the fourth- and ther second-order fiber-orientation tensors, $\bar{\mathbb{N}}$ and $\bar{\boldsymbol{N}}=\bar{\mathbb{N}}[\mathbf{1}]$, respectively (for their definitions see section 2.1.1). The assumption that

the viscosity parameters are independent of the fiber-orientation state is discussed in section 6.3.

2.3 Modeling approach

The fiber-orientation evolution-models and the effective-viscosity models described in this work may serve as input for form-filling simulations, e.g., (Ospald, 2014; Buck et al., 2015; Bertóti and Böhlke, 2017a; Köbler et al., 2018). The fiber motion induced by the fluid flow (fluid→fiber interaction) is generally modeled by Jeffery's equation (Jeffery, 1922; Junk and Illner, 2007), as described in Chapter 3. Concerning a momentary fiber-orientation state, the back-coupling, i.e., the influence of the actual fiber orientation on the fluid motion (fiber→fluid interaction) is mostly neglected in form-filling simulations. One possible way to account for the back-coupling is to describe the fluid-fiber suspension by the effective tensorial viscosity which depends on the microstructure properties and especially on the actual fiber-orientation state. Neglecting the tensorial nature of the effective viscosity in the form-filling simulations has different reasons:

1. Computing with isotropic effective viscosity, with the use of fitting parameters in the fiber-orientation evolution-models is already a challenging and complex task, without the consideration of the anisotropy of the viscosity.
2. Most fluid dynamics codes are numerically optimized for isotropic viscosity but not for anisotropic, i.e., tensorial viscosity.
3. Experimental validation of a tensorial viscosity model prediction is quite difficult, because of the continuously re-orientating fibers. Such a work is not known to the author.

Tensorial effective material models, e.g., (Hinch and Leal, 1972; Mori and

Tanaka, 1973; Shaqfeh and Fredrickson, 1990), applied for the viscosity, give predictions for the three viscosity parameters, see Chapter 4. To overcome the lack of real experiments, numerical full-field simulations are carried out – which can be considered as numerical experiments – to determine the viscosity parameters in this way, see Chapter 5. The numerical results are used to prove the theoretical model predictions and to give improved approximations of $\bar{\mathbb{V}}$, considering also the size of the homogenized volume element and the spatial distribution of the fibers in it, see Chapter 6.

Chapter 3

Flow-induced anisotropy of the fiber orientation [1]

3.1 Jeffery's equation

Jeffery (1922) described a single fiber with its normalized direction vector $\boldsymbol{n}_\alpha$, where $\alpha = 1, 2, \ldots, M$ denotes the index of the fiber. The evolution equation of $\boldsymbol{n}_\alpha$ is given by

$$\dot{\boldsymbol{n}}_\alpha = \bar{\boldsymbol{W}}[\boldsymbol{n}_\alpha] + \xi(\bar{\boldsymbol{D}}[\boldsymbol{n}_\alpha] - (\boldsymbol{n}_\alpha \otimes \boldsymbol{n}_\alpha \otimes \boldsymbol{n}_\alpha)[\bar{\boldsymbol{D}}]), \quad \xi = \frac{r_\mathrm{a}^2 - 1}{r_\mathrm{a}^2 + 1}\,,\ r_\mathrm{a} = l/d, \tag{3.1}$$

where $\bar{\boldsymbol{W}}$ is the effective vorticity tensor, and $\bar{\boldsymbol{D}}$ is the effective strain rate tensor, being the skew-symmetric and the symmetric parts of the effective velocity gradient $\bar{\boldsymbol{L}} = \partial\bar{\boldsymbol{v}}/\partial\boldsymbol{x}$, respectively. The parameter $\xi \in (0, 1)$ describes the geometry of the fibers, determined by the aspect-ratio r_a, the fiber length l and the fiber diameter d. For fibers $\xi \approx 1$. A modern derivation of (3.1) is given by Junk and Illner (2007).

With the use of the dilute distribution approximation – which assumes that the fibers do not interact with each other – Jeffery's equation separately describes the motion of all M fibers in a viscous flow. In the Figures 3.1-3.4 the fiber-orientation evolutions of $M = 1000$ randomly generated, initially equally distributed (Mardia and Jupp, 2009) fibers are

[1] This chapter is based on Bertóti and Böhlke (2017b).

represented, considering slender fibers ($r_\mathrm{a} \to \infty, \xi \to 1$). The following four representative, isochoric flow modes are considered: shear flow (sf), elongational flow (ef), compressional flow (cf), and a planar flow (pf) which is the superposition of an elongational and a compressional flow. The corresponding velocity gradients are given by

$$\begin{aligned} \bar{\boldsymbol{L}}^{\mathrm{sf}} &\hat{=} \begin{pmatrix} 0 & b & 0 \\ 0 & 0 & 0 \\ 0 & 0 & 0 \end{pmatrix}, \qquad \bar{\boldsymbol{L}}^{\mathrm{ef}} \hat{=} \begin{pmatrix} b & 0 & 0 \\ 0 & -\frac{b}{2} & 0 \\ 0 & 0 & -\frac{b}{2} \end{pmatrix}, \\ \bar{\boldsymbol{L}}^{\mathrm{cf}} &\hat{=} \begin{pmatrix} -b & 0 & 0 \\ 0 & \frac{b}{2} & 0 \\ 0 & 0 & \frac{b}{2} \end{pmatrix}, \quad \bar{\boldsymbol{L}}^{\mathrm{pf}} \hat{=} \begin{pmatrix} b & 0 & 0 \\ 0 & -b & 0 \\ 0 & 0 & 0 \end{pmatrix}, \end{aligned} \tag{3.2}$$

where b is an arbitrary scalar factor with dimension s^{-1}. The Figures 3.1-3.8 are generated with $b = 1\ \mathrm{s}^{-1}$, and they depict the deformation states from left to right $\bar{\varepsilon}_\mathrm{M} = 0, \bar{\varepsilon}_\mathrm{M} = 3, \bar{\varepsilon}_\mathrm{M} = 6$ and the quasi-stationary $\bar{\varepsilon}_\mathrm{M} = 9$. The variable $\bar{\varepsilon}_\mathrm{M}$ denotes the chosen scalar deformation measure, i.e., the effective von Mises equivalent strain, defined by

$$\bar{\varepsilon}_\mathrm{M}(t) = \int_0^t \dot{\bar{\varepsilon}}_\mathrm{M} \mathrm{d}t, \quad \dot{\bar{\varepsilon}}_\mathrm{M} = \sqrt{\frac{2}{3}} \left\| \bar{\boldsymbol{D}}' \right\|. \tag{3.3}$$

which also depends on the magnitude of the parameter b. For generating the Figures 3.1-3.8 an explicit Euler method is used:

$$\bar{\varepsilon}_\mathrm{M}(t+\Delta t) = \bar{\varepsilon}_\mathrm{M}(t) + \dot{\bar{\varepsilon}}_\mathrm{M}(t)\Delta t, \quad \boldsymbol{n}_\alpha(t+\Delta t) = \frac{\boldsymbol{n}_\alpha(t) + \dot{\boldsymbol{n}}_\alpha(t)\Delta t}{\|\boldsymbol{n}_\alpha(t) + \dot{\boldsymbol{n}}_\alpha(t)\Delta t\|}. \tag{3.4}$$

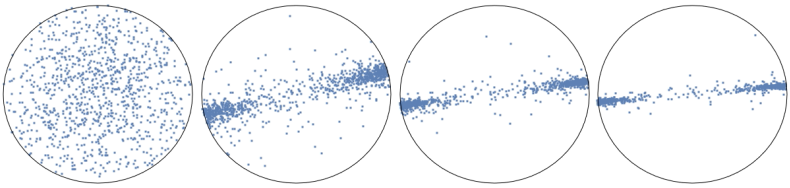

Figure 3.1: Pole figures of 1000 fibers in a shear flow (Bertóti and Böhlke, 2017b).

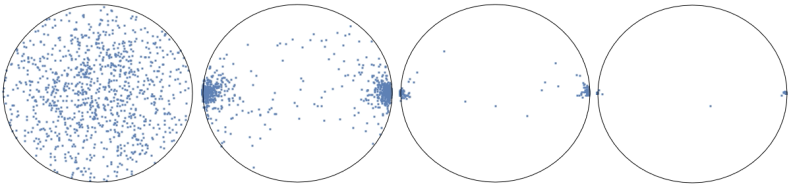

Figure 3.2: Pole figures of 1000 fibers in an elongational flow (Bertóti and Böhlke, 2017b).

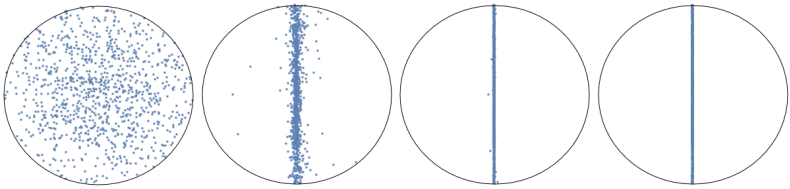

Figure 3.3: Pole figures of 1000 fibers in a compressional flow (Bertóti and Böhlke, 2017b).

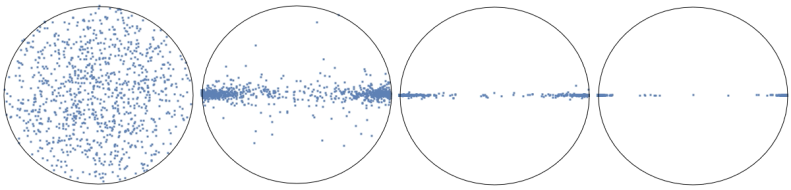

Figure 3.4: Pole figures of 1000 fibers in a planar flow (Bertóti and Böhlke, 2017b).

The velocity gradient is considered to be constant. For this reason, the numerically computed $\bar{\varepsilon}_{\mathrm{M}}$ is exact. The time increment Δt was decreased until the computations with the time step sizes $2\Delta t$, Δt and $\Delta t/2$ gave similar results.

Each of the Figures 3.1-3.4 belongs to one of the investigated flow modes. The last pole figures in a row ($\bar{\varepsilon}_{\mathrm{M}} = 9$) indicate that the quasi-stationary orientation state for the shear flow and for the compressional flow is nearly planar and planar, respectively. The quasi-stationary orientation state for the elongational flow and for the planar flow is unidirectional and nearly unidirectional, respectively. A periodic solution does not appear here, because the aspect ratio of the representative fiber is set to infinity. For this case, the stationary solution is also stated, e.g., by Jeffery (1922) and Junk and Illner (2007). Approximating the fiber reorientations by fiber-orientation tensors is discussed in the next section.

3.2 Tensor form of Jeffery's equation

Applying orientation averaging to (3.1) results the second-order tensor form of Jeffery's equation:

$$\dot{\bar{\boldsymbol{N}}} = \bar{\boldsymbol{W}}\bar{\boldsymbol{N}} - \bar{\boldsymbol{N}}\bar{\boldsymbol{W}} + \xi(\bar{\boldsymbol{D}}\bar{\boldsymbol{N}} + \bar{\boldsymbol{N}}\bar{\boldsymbol{D}} - 2\bar{\mathbb{N}}[\bar{\boldsymbol{D}}]), \tag{3.5}$$

where $\bar{\mathbb{N}}$ denotes the fourth-order fiber-orientation tensor which can be determined directly from the $\boldsymbol{n}_\alpha$-s, as defined in equation (2.4), or it can be approximated – e.g., by a closure approximation (see section 3.3) – if fast computations without tracking each of the M fibers are wanted. An alternative representation of (3.5) with the objective Jaumann-Zaremba rate is given by $\mathring{\bar{\boldsymbol{N}}}^{\mathrm{JZ}} = \dot{\bar{\boldsymbol{N}}} - \bar{\boldsymbol{W}}\bar{\boldsymbol{N}} + \bar{\boldsymbol{N}}\bar{\boldsymbol{W}}$ (Holzapfel, 2000; Wang et al., 2008). The anisotropy of $\bar{\boldsymbol{N}}$ is measured by the norm $||\bar{\boldsymbol{N}}^{\mathrm{aniso}}||$, where

$$\bar{\boldsymbol{N}}^{\mathrm{aniso}} = \bar{\boldsymbol{N}} - \bar{\boldsymbol{N}}^{\mathrm{iso}}, \quad \bar{\boldsymbol{N}}^{\mathrm{iso}} = \frac{1}{3}(\bar{\boldsymbol{N}} \cdot \mathbf{1})\mathbf{1}. \tag{3.6}$$

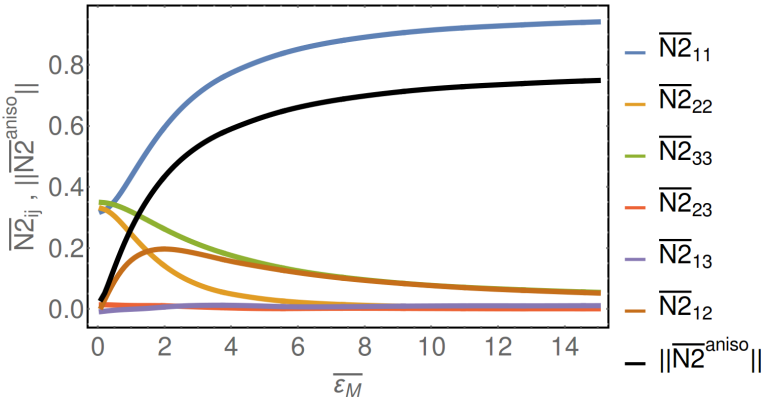

Figure 3.5: Shear flow: evolution of the components $\bar{N}_{ij}$ and the anisotropy norm $||\bar{\boldsymbol{N}}^{\text{aniso}}||$ of the second-order fiber-orientation tensor $\bar{\boldsymbol{N}}$ (Bertóti and Böhlke, 2017b).

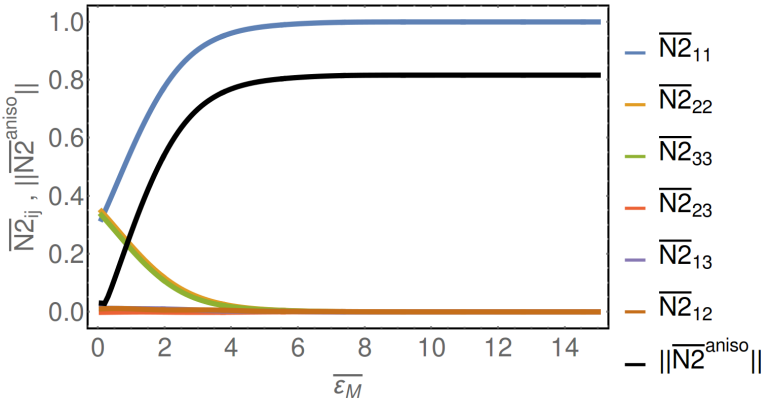

Figure 3.6: Elongational flow: evolution of the components $\bar{N}_{ij}$ and the anisotropy norm $||\bar{\boldsymbol{N}}^{\text{aniso}}||$ of the second-order fiber-orientation tensor $\bar{\boldsymbol{N}}$ (Bertóti and Böhlke, 2017b).

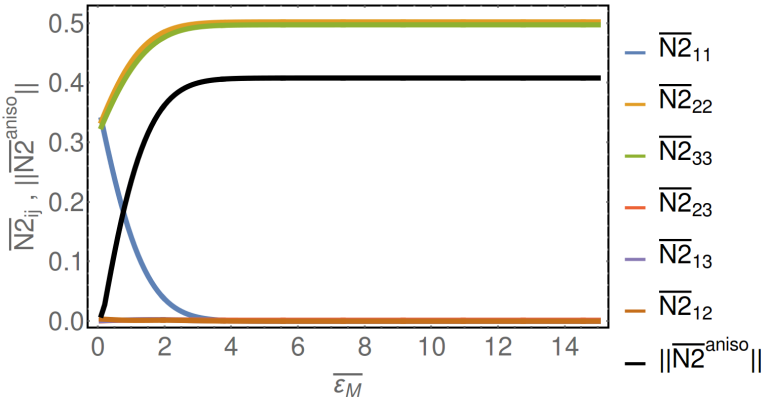

Figure 3.7: Compressional flow: evolution of the components $\bar{N}_{ij}$ and the anisotropy norm $||\bar{\boldsymbol{N}}^{\text{aniso}}||$ of the second-order fiber-orientation tensor $\bar{\boldsymbol{N}}$ (Bertóti and Böhlke, 2017b).

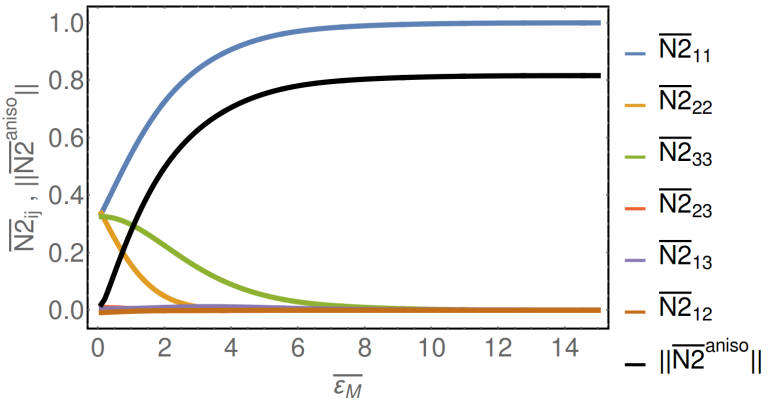

Figure 3.8: Planar flow: evolution of the components $\bar{N}_{ij}$ and the anisotropy norm $||\bar{\boldsymbol{N}}^{\text{aniso}}||$ of the second-order fiber-orientation tensor $\bar{\boldsymbol{N}}$ (Bertóti and Böhlke, 2017b).

The Figures 3.5-3.8 show the evolution of the components $\bar{N}_{ij}$ and of the anisotropy norm $||\bar{\boldsymbol{N}}^{\text{aniso}}||$ depending on $\bar{\varepsilon}_M$, computed by the discrete (disc) model, considering the four investigated flow modes. In all four flow cases, the initial ($\bar{\varepsilon}_M = 0$) fiber-orientation state is isotropic ($||\bar{\boldsymbol{N}}^{\text{aniso}}|| = 0$). It is observed that the slowest anisotropy increase is caused by the shear flow ($||\bar{\boldsymbol{N}}^{\text{aniso}}_{\text{sf}}||_{\text{max}} = ||\bar{\boldsymbol{N}}^{\text{aniso}}_{\text{sf}}(\bar{\varepsilon}_M = 15)|| = 0.75$) and the fastest anisotropy increase is caused by the compressional flow ($||\bar{\boldsymbol{N}}^{\text{aniso}}_{\text{cf}}||_{\text{max}} = ||\bar{\boldsymbol{N}}^{\text{aniso}}_{\text{cf}}(\bar{\varepsilon}_M \geq 3)|| = 0.8$).

3.3 Investigated closure approximations

Two of the various closure approximations are investigated for computations without tracking all of the M fibers. The simplest one is the quadratic closure (Doi, 1981)

$$\bar{\mathbb{N}}^{\text{quad}} = \bar{\boldsymbol{N}} \otimes \bar{\boldsymbol{N}} \tag{3.7}$$

which is only exact for aligned fibers. The invariant-based optimal fitting (Chung and Kwon, 2002a)

$$\begin{aligned} \bar{\mathbb{N}}^{\text{IBOF}} \quad = \quad & \bar{\beta}_1 \, \text{S}(\mathbf{1} \otimes \mathbf{1}) + \bar{\beta}_2 \, \text{S}(\mathbf{1} \otimes \bar{\boldsymbol{N}}) + \bar{\beta}_3 \, \text{S}(\bar{\boldsymbol{N}} \otimes \bar{\boldsymbol{N}}) + \\ & \bar{\beta}_4 \, \text{S}(\mathbf{1} \otimes \bar{\boldsymbol{N}}\bar{\boldsymbol{N}}) + \bar{\beta}_5 \, \text{S}(\bar{\boldsymbol{N}} \otimes \bar{\boldsymbol{N}}\bar{\boldsymbol{N}}) + \bar{\beta}_6 \, \text{S}(\bar{\boldsymbol{N}}\bar{\boldsymbol{N}} \otimes \bar{\boldsymbol{N}}\bar{\boldsymbol{N}}) \end{aligned} \tag{3.8}$$

is more complex but also more realistic. In the case of closure approximations, the numerical integration of equation (3.5) is computed analogously to equation (3.4) as

$$\bar{\boldsymbol{N}}(t + \Delta t) = \frac{\bar{\boldsymbol{N}}(t) + \dot{\bar{\boldsymbol{N}}}(t)\Delta t}{\text{tr}(\bar{\boldsymbol{N}}(t) + \dot{\bar{\boldsymbol{N}}}(t)\Delta t)}. \tag{3.9}$$

The term in the denominator ensures that the new second-order fiber-orientation tensor has also unit trace.

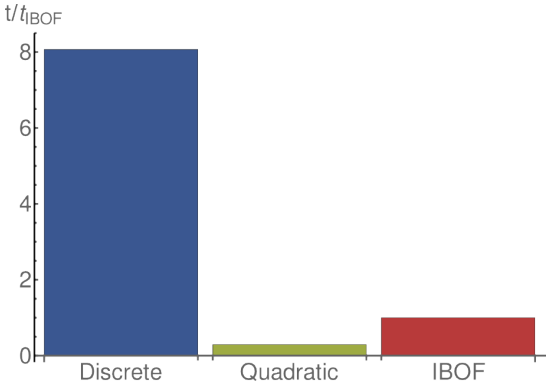

Figure 3.9: Relative computation times of the investigated models (Bertóti and Böhlke, 2017b).

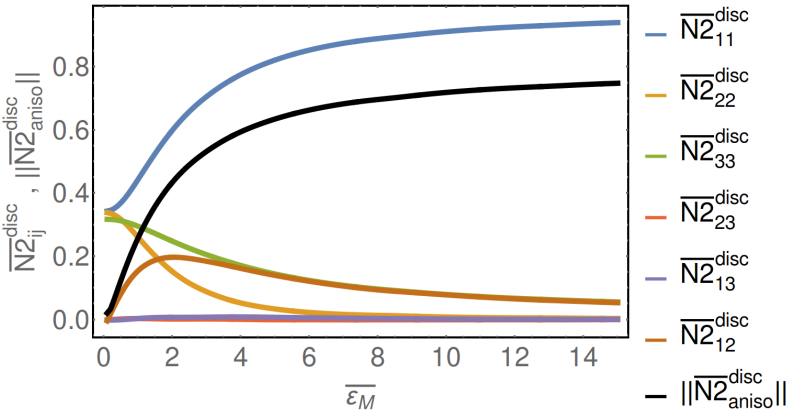

Figure 3.10: Discrete model, $M = 1000$: Evolution of the components $\bar{N}_{ij}$ and the anisotropy norm $||\bar{\boldsymbol{N}}^{\text{aniso}}||$ of the second-order fiber-orientation tensor $\bar{\boldsymbol{N}}$ in a shear flow (Bertóti and Böhlke, 2017b).

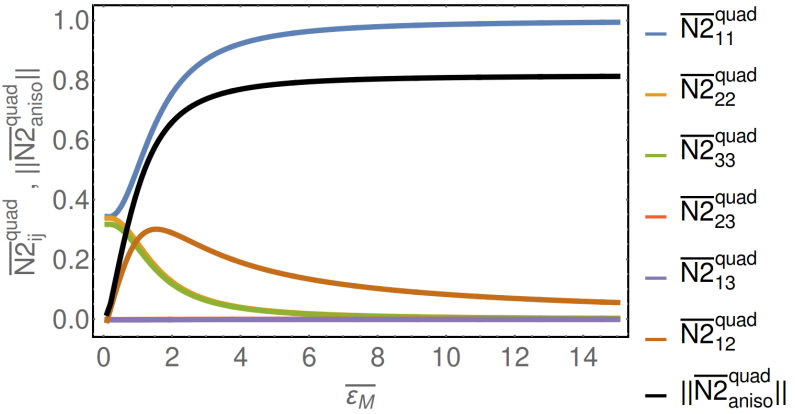

Figure 3.11: Quadratic model: Evolution of the components $\bar{N}_{ij}$ and the anisotropy norm $||\bar{\boldsymbol{N}}^{\text{aniso}}||$ of the second-order fiber-orientation tensor $\bar{\boldsymbol{N}}$ in a shear flow (Bertóti and Böhlke, 2017b).

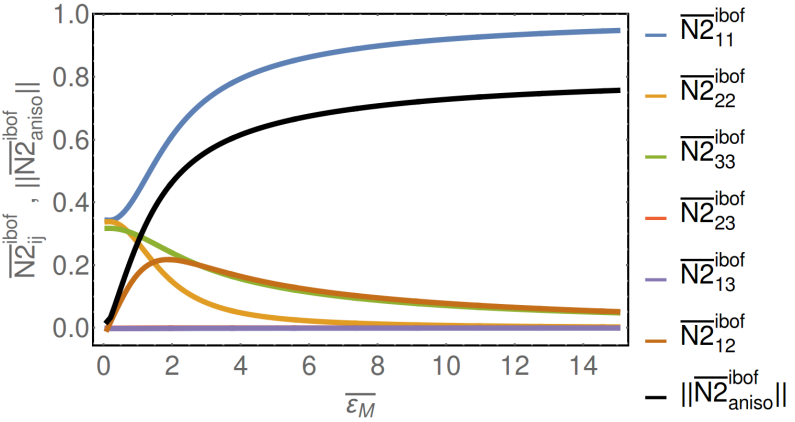

Figure 3.12: IBOF model: Evolution of the components $\bar{N}_{ij}$ and the anisotropy norm $||\bar{\boldsymbol{N}}^{\text{aniso}}||$ of the second-order fiber-orientation tensor $\bar{\boldsymbol{N}}$ in a shear flow (Bertóti and Böhlke, 2017b).

A notable difference is observed considering the relative computation times of the discrete, the quadratic and that of the IBOF model, see Figure 3.9. The discrete model with the $M = 1000$ fibers is about 8 times slower, and the model with the quadratic closure about 3 times faster than the model with the IBOF closure. Although the model with the quadratic closure is the fastest, its use is not recommended, because it provides qualitatively different results for the transient change than the discrete model, which is regarded as the validating reference (compare Figures 3.10 and 3.11). The reason for the qualitative difference is that the quadratic closure is exact only for highly aligned fibers, but not for general fiber-orientation distributions. Computing with the IBOF closure is slower than computing with the quadratic closure, but the IBOF closure provides qualitatively the same results as the discrete reference model, also during the transient change (compare Figures 3.10 and 3.12). The differences and similarities are depicted here only for the shear flow (3.2), but similar qualitative differences and similarities are observed also for the three other investigated flow modes. Because of the above mentioned reasons, using of the fiber-orientation tensors with the IBOF closure is recommended, as also stated in, e.g., Chung and Kwon (2002a).

In this chapter the evolution of the flow-induced anisotropy in short-fiber suspensions was demonstrated. In the following, fiber-orientation states at fixed times are investigated. The goal is to determine the anisotropic effective viscosity $\bar{\mathbb{V}}$ of the momentary fiber-orientation states, first by mean-field homogenization (Chapter 4) and then by full-field homogenization (Chapter 5).

Chapter 4

Mean-field homogenization of viscous properties

4.1 Mean-field homogenization using Mori-Tanaka's method based on Eshelby's tensor

Scale separation, ergodicity and the existence of a representative volume element V is assumed (Torquato, 2002). Two-phase materials made up of piecewise constant, isotropic and linear viscous constituents are considered. Taking these assumptions into account the exact effective viscosity $\bar{\mathbb{V}}$ is determined by the volume average of the local viscosity tensor $\mathbb{V}$ and the strain-rate localization tensor $\mathbb{A}$

$$\bar{\mathbb{V}} = \langle \mathbb{V}\mathbb{A} \rangle = \frac{1}{V} \int_V \mathbb{V}\mathbb{A} \mathrm{d}V, \tag{4.1}$$

where $\mathbb{A}$ describes the relationship between the strain rate on the microscopic scale and the macroscopic scale $\boldsymbol{D} = \mathbb{A}[\bar{\boldsymbol{D}}]$, and $\mathbb{V}$ is the viscosity on the microscopic scale for the microscopic stress $\boldsymbol{\sigma} = \mathbb{V}[\boldsymbol{D}]$. The macroscopic stress $\bar{\boldsymbol{\sigma}} = \langle \boldsymbol{\sigma} \rangle$ and the macroscopic strain rate $\bar{\boldsymbol{D}} = \langle \boldsymbol{D} \rangle$ are volume averages of the corresponding microscopic measures due to the assumption of ergodicity.

When the two-phase material is specified by rigid fibers immersed in an incompressible viscous fluid matrix with piecewise constant, isotropic

and linear viscosities $\mathbb{V}_\mathrm{f} = \eta_\mathrm{f}\mathbb{P}_2$ and $\mathbb{V}_\mathrm{m} = \eta_\mathrm{m}\mathbb{P}_2$, then (4.1) reduces to

$$\bar{\mathbb{V}} = c_\mathrm{m}\mathbb{V}_\mathrm{m}\mathbb{A}_\mathrm{m} + c_\mathrm{f}\mathbb{V}_\mathrm{f}\mathbb{A}_\mathrm{f}, \tag{4.2}$$

where c_f is the fiber volume fraction, $c_\mathrm{m} = 1 - c_\mathrm{f}$ is the matrix volume fraction, and $\mathbb{A}_\mathrm{m} = \langle\mathbb{A}\rangle_\mathrm{m}$, $\mathbb{A}_\mathrm{f} = \langle\mathbb{A}\rangle_\mathrm{f}$ are the phase averages of the strain-rate localization tensor $\mathbb{A}$ for the fibers (f) and the matrix (m). The scalars η_m and η_f are the shear viscosities of the matrix and the fiber, respectively, and $\mathbb{P}_2$ is the second projector tensor of fourth order (see section 2.1). Due to the normalization condition $\mathbb{I}^\mathrm{s} = c_\mathrm{m}\mathbb{A}_\mathrm{m} + c_\mathrm{f}\mathbb{A}_\mathrm{f}$, $\mathbb{A}_\mathrm{m}$ can be expressed as

$$\mathbb{A}_\mathrm{m} = \frac{1}{c_\mathrm{m}}(\mathbb{I}^\mathrm{s} - c_\mathrm{f}\mathbb{A}_\mathrm{f}). \tag{4.3}$$

Substituting (4.3) into (4.2), we get

$$\bar{\mathbb{V}} = \mathbb{V}_\mathrm{m} + c_\mathrm{f}(\mathbb{V}_\mathrm{f} - \mathbb{V}_\mathrm{m})\mathbb{A}_\mathrm{f}. \tag{4.4}$$

Using Mori-Tanaka's method (Mori and Tanaka, 1973), $\mathbb{A}_\mathrm{f}$ is estimated by

$$\mathbb{A}_\mathrm{f}^\mathrm{MT} = (c_\mathrm{f}\mathbb{I}^\mathrm{s} + c_\mathrm{m}\mathbb{A}_\mathrm{f}^\infty)^{-1} = \left(\mathbb{I}^\mathrm{s} + c_\mathrm{m}\mathbb{E}_\mathrm{m}\mathbb{V}_\mathrm{m}^{-1}(\mathbb{V}_\mathrm{f} - \mathbb{V}_\mathrm{m})\right)^{-1}, \tag{4.5}$$

where $\mathbb{A}_\mathrm{f}^\infty = \mathbb{I}^\mathrm{s} + \mathbb{E}_\mathrm{m}\mathbb{V}_\mathrm{m}^{-1}(\mathbb{V}_\mathrm{f} - \mathbb{V}_\mathrm{m})$ is the influence tensor (Gross and Seelig, 2017), and $\mathbb{E}_\mathrm{m}$ is Eshelby's tensor depending on the matrix material properties (Eshelby, 1957). Substituting (4.5) into (4.4), we get the approximation of $\bar{\mathbb{V}}$ using Mori-Tanaka's method

$$\begin{aligned}\bar{\mathbb{V}}^\mathrm{MT} &= \mathbb{V}_\mathrm{m} + c_\mathrm{f}(\mathbb{V}_\mathrm{f} - \mathbb{V}_\mathrm{m})\left(\mathbb{I}^\mathrm{s} + c_\mathrm{m}\mathbb{E}_\mathrm{m}\mathbb{V}_\mathrm{m}^{-1}(\mathbb{V}_\mathrm{f} - \mathbb{V}_\mathrm{m})\right)^{-1} &(4.6)\\ &= \mathbb{V}_\mathrm{m} + c_\mathrm{f}\left((\mathbb{V}_\mathrm{f} - \mathbb{V}_\mathrm{m})^{-1} + c_\mathrm{m}\mathbb{E}_\mathrm{m}\mathbb{V}_\mathrm{m}^{-1}\right)^{-1}. &(4.7)\end{aligned}$$

The fibers are assumed to be rigid, as discussed in section 2.1, i.e., they are infinitely viscous $\mathbb{V}_\mathrm{f} = 2\eta_\mathrm{f}\mathbb{P}_2$, $\eta_\mathrm{f} = \infty$ which implies that

$(\mathbb{V}_\mathrm{f} - \mathbb{V}_\mathrm{m})^{-1} = 0$ and

$$\bar{\mathbb{V}}^{\mathrm{MT}} = \mathbb{V}_\mathrm{m} + \frac{c_\mathrm{f}}{c_\mathrm{m}} \left(\mathbb{E}_\mathrm{m}\mathbb{V}_\mathrm{m}^{-1}\right)^{-1} = \mathbb{V}_\mathrm{m} + \frac{c_\mathrm{f}}{c_\mathrm{m}}\mathbb{P}_0^{-1}, \tag{4.8}$$

where $\mathbb{P}_0 = \mathbb{E}_\mathrm{m}\mathbb{V}_\mathrm{m}^{-1}$ is the polarization tensor (Walpole, 1969; Castaneda and Suquet, 1997). For infinitely viscous fibers ($\eta_\mathrm{f} = \infty$), the same form is obtained by using the Hashin-Strikman lower bound (Hashin and Shtrikman, 1962; Willis, 1977).

4.2 Microstructure dependence of the transversely isotropic viscosity parameters

The approximation of the unidirectional, i.e., a transversely isotropic, effective viscosity tensor $\bar{\mathbb{V}}_\mathrm{ud}$ based on the Mori-Tanaka homogenization scheme (Mori and Tanaka, 1973) and the unidirectional Eshelby tensor $\mathbb{E}_\mathrm{ud}$ for a spheroidal fiber inclusion (Eshelby, 1957; Tandon and Weng, 1984), considering infinitely viscous fibers ($\eta_\mathrm{f} = \infty$) immersed in a purely viscous matrix with shear viscosity η_m has the form

$$\bar{\mathbb{V}}_\mathrm{ud} = 2\eta_\mathrm{m}\left(\mathbb{P}_2 + \frac{\bar{c}_\mathrm{f}}{1-\bar{c}_\mathrm{f}}\mathbb{E}_\mathrm{ud}^{-1}\right), \tag{4.9}$$

analogously to (4.8), where $\bar{c}_\mathrm{f}$ is the fiber volume fraction and $\mathbb{P}_2$ is the second projector tensor of fourth order (see section 2.1).

A fourth-order transversely isotropic tensor $\mathbb{T}$ with symmetry axis $\boldsymbol{n}$ has, in general, five independent scalar parameters (Spencer et al., 1984; Boehler, 1987; Fiolka, 2008; Weise and Meyer, 2010), denoted here by $\lambda_1, \lambda_2, \mu, \alpha, \beta$. In the case of incompressibility, only three of

them (μ, α, β) are left, such that

$$\begin{aligned}
\mathbb{T}'(\mu,\alpha,\beta,\boldsymbol{n}) &= \mathbb{P}_2\mathbb{T}(\lambda_1,\lambda_2,\mu,\alpha,\beta,\boldsymbol{n})\mathbb{P}_2 \\
&= \mathbb{P}_2(\lambda_1\mathbb{P}_1 + \lambda_2(\boldsymbol{n}^{\otimes 2}\otimes\mathbf{1} + \mathbf{1}\otimes\boldsymbol{n}^{\otimes 2}) \\
&\quad +2\mu\mathbb{P}_2 + \alpha\left(\boldsymbol{n}^{\otimes 2}\square\mathbf{1} + \mathbf{1}\square\boldsymbol{n}^{\otimes 2}\right) + \beta\boldsymbol{n}^{\otimes 4})\mathbb{P}_2 \\
&= 2\mu\mathbb{P}_2 + \alpha(\boldsymbol{n}^{\otimes 2}\square\mathbf{1} + \mathbf{1}\square\boldsymbol{n}^{\otimes 2} \\
&\quad -\frac{2}{3}\left(\mathbf{1}\otimes\boldsymbol{n}^{\otimes 2} + \boldsymbol{n}^{\otimes 2}\otimes\mathbf{1}\right) + \frac{2}{9}\left(\mathbf{1}\otimes\mathbf{1}\right)) \\
&\quad +\beta\left(\boldsymbol{n}^{\otimes 4} - \frac{1}{3}\left(\mathbf{1}\otimes\boldsymbol{n}^{\otimes 2} + \boldsymbol{n}^{\otimes 2}\otimes\mathbf{1}\right) + \frac{1}{9}\left(\mathbf{1}\otimes\mathbf{1}\right)\right),
\end{aligned} \tag{4.10}$$

where $\boldsymbol{n}^{\otimes 2} = \boldsymbol{n}\otimes\boldsymbol{n}$ and $\boldsymbol{n}^{\otimes 4} = \boldsymbol{n}\otimes\boldsymbol{n}\otimes\boldsymbol{n}\otimes\boldsymbol{n}$. Since $\mathbb{E}_{\text{ud}}$, $\mathbb{E}_{\text{ud}}^{-1}$ and $\bar{\mathbb{V}}_{\text{ud}}$ are all fourth-order transversely isotropic tensors, they can be written as

$$\begin{aligned}
\mathbb{E}_{\text{ud}} &= \mathbb{T}'(\mu_{\text{E}},\alpha_{\text{E}},\beta_{\text{E}},\boldsymbol{n}), \\
\mathbb{E}_{\text{ud}}^{-1} &= \mathbb{T}'(\mu_{\text{E}}^*,\alpha_{\text{E}}^*,\beta_{\text{E}}^*,\boldsymbol{n}), \\
\bar{\mathbb{V}}_{\text{ud}} &= \mathbb{T}'(\bar{\mu}_{\text{V}},\bar{\alpha}_{\text{V}},\bar{\beta}_{\text{V}},\boldsymbol{n}).
\end{aligned} \tag{4.11}$$

Using the formulas for Eshelby's tensor given by, e.g., Tandon and Weng (1984), with $\nu_0 = 0.5$, which corresponds to the considered incompressibility, we get

$$\mu_{\text{E}} = \frac{r_{\text{a}}^2 - h}{4(r_{\text{a}}^2 - 1)}, \tag{4.12}$$

$$\alpha_{\text{E}} = \frac{r_{\text{a}}^2 + 1}{r_{\text{a}}^2 - 1}(h-1) - 2\mu_{\text{E}}, \tag{4.13}$$

$$\beta_{\text{E}} = \frac{3}{4}\frac{(5-4h)r_{\text{a}}^2 - h}{(r_{\text{a}}^2 - 1)} - 2\alpha_{\text{E}}, \tag{4.14}$$

$$h = \frac{3}{2}\frac{r_{\text{a}}\left(r_{\text{a}}\sqrt{r_{\text{a}}^2 - 1} - \cosh^{-1}(r_{\text{a}})\right)}{(r_{\text{a}}^2 - 1)^{3/2}}, \tag{4.15}$$

where r_a is the aspect ratio of the ellipsoidal inclusion, i.e., of the fiber. The three scalar parameters for the inverse of Eshelby's tensor are determined by

$$\mu_\mathrm{E}^* = \frac{1}{4\mu_\mathrm{E}}, \tag{4.16}$$

$$\alpha_\mathrm{E}^* = -\frac{\alpha_\mathrm{E}}{2\mu_\mathrm{E}(2\mu_\mathrm{E}+\alpha_\mathrm{E})}, \tag{4.17}$$

$$\beta_\mathrm{E}^* = \frac{\frac{2}{3}\alpha_\mathrm{E}(\alpha_\mathrm{E}+2\beta_\mathrm{E}) - \beta_\mathrm{E}(2\mu_\mathrm{E}+\alpha_\mathrm{E})}{2\mu_\mathrm{E}(2\mu_\mathrm{E}+\alpha_\mathrm{E})\left(2\mu_\mathrm{E}+\frac{2}{3}(2\alpha_\mathrm{E}+\beta_\mathrm{E})\right)}. \tag{4.18}$$

Substituting the equations (4.16)-(4.18) into (4.9)-(4.11), the three scalar parameters for $\bar{\mathbb{V}}_\mathrm{ud}$ are identified as

$$\bar{\mu}_\mathrm{V} = \eta^\mathrm{m}\left(1+\frac{\bar{c}_\mathrm{f}}{1-\bar{c}_\mathrm{f}}2\mu_\mathrm{E}^*\right), \tag{4.19}$$

$$\bar{\alpha}_\mathrm{V} = 2\eta^\mathrm{m}\frac{\bar{c}_\mathrm{f}}{1-\bar{c}_\mathrm{f}}\alpha_\mathrm{E}^*, \tag{4.20}$$

$$\bar{\beta}_\mathrm{V} = 2\eta^\mathrm{m}\frac{\bar{c}_\mathrm{f}}{1-\bar{c}_\mathrm{f}}\beta_\mathrm{E}^*. \tag{4.21}$$

The viscosity parameters $\bar{\eta}, \bar{N}_\mathrm{s}, \bar{N}_\mathrm{p}$ for the common parametrization (2.11) of the transversely isotropic viscosity tensor are determined by

$$\bar{\eta} = \bar{\mu}_\mathrm{V}, \tag{4.22}$$

$$\bar{N}_\mathrm{s} = \frac{\bar{\alpha}_\mathrm{V}}{2\bar{\eta}}, \tag{4.23}$$

$$\bar{N}_\mathrm{p} = \frac{\bar{\beta}_\mathrm{V}}{2\bar{\eta}}. \tag{4.24}$$

Substituting (4.12)-(4.21) into (4.24) yields

$$\bar{\eta} = \eta_{\mathrm{m}}\left(1+\frac{2\bar{c}_{\mathrm{f}}}{(1-\bar{c}_{\mathrm{f}})}\frac{2(r_{\mathrm{a}}^2-1)^{5/2}}{\left(2r_{\mathrm{a}}^2(r_{\mathrm{a}}^2-1)^{3/2}-3r_{\mathrm{a}}\left(r_{\mathrm{a}}\sqrt{r_{\mathrm{a}}^2-1}-\cosh^{-1}(r_{\mathrm{a}})\right)\right)}\right), \tag{4.25}$$

$$\bar{N}_{\mathrm{s}} = \frac{\bar{c}_{\mathrm{f}}}{\left(\sqrt{r_{\mathrm{a}}^2-1}\,(2r_{\mathrm{a}}^4(\bar{c}_{\mathrm{f}}+1)-r_{\mathrm{a}}^2(3\bar{c}_{\mathrm{f}}+5)+4\bar{c}_{\mathrm{f}})-3r_{\mathrm{a}}(\bar{c}_{\mathrm{f}}-1)\cosh^{-1}(r_{\mathrm{a}})\right)}\frac{6r_{\mathrm{a}}\left(r_{\mathrm{a}}^2-1\right)^{5/2}\left(2r_{\mathrm{a}}^2+3\right)\cosh^{-1}(r_{\mathrm{a}})-2\left(r_{\mathrm{a}}^2-1\right)^3\left(11r_{\mathrm{a}}^2+4\right)}{(r_{\mathrm{a}}^2+1)\left(\sqrt{r_{\mathrm{a}}^2-1}\,(r_{\mathrm{a}}^2+2)-3r_{\mathrm{a}}\cosh^{-1}(r_{\mathrm{a}})\right)}, \tag{4.26}$$

$$\begin{aligned}\bar{N}_{\mathrm{p}} = {} & \frac{\bar{c}_{\mathrm{f}}}{\left(\sqrt{r_{\mathrm{a}}^2-1}\,(2r_{\mathrm{a}}^4(\bar{c}_{\mathrm{f}}+1)-r_{\mathrm{a}}^2(3\bar{c}_{\mathrm{f}}+5)+4\bar{c}_{\mathrm{f}})-3r_{\mathrm{a}}(\bar{c}_{\mathrm{f}}-1)\cosh^{-1}(r_{\mathrm{a}})\right)}\\ & \frac{\left(r_{\mathrm{a}}^2-1\right)^{5/2}}{(r_{\mathrm{a}}^2+1)}\frac{\left(\sqrt{r_{\mathrm{a}}^2-1}\left(r_{\mathrm{a}}^2+2\right)-3r_{\mathrm{a}}\cosh^{-1}(r_{\mathrm{a}})\right)^{-1}}{\left(-3\sqrt{r_{\mathrm{a}}^2-1}r_{\mathrm{a}}+2r_{\mathrm{a}}^2\cosh^{-1}(r_{\mathrm{a}})+\cosh^{-1}(r_{\mathrm{a}})\right)}\\ & \Big(r_{\mathrm{a}}\left(2r_{\mathrm{a}}^8+17r_{\mathrm{a}}^6-108r_{\mathrm{a}}^4+67r_{\mathrm{a}}^2+22\right)\\ & -3r_{\mathrm{a}}\left(4r_{\mathrm{a}}^4+17r_{\mathrm{a}}^2+9\right)\cosh^{-1}(r_{\mathrm{a}})^2\\ & -2\sqrt{r_{\mathrm{a}}^2-1}\left(9r_{\mathrm{a}}^6-38r_{\mathrm{a}}^4-56r_{\mathrm{a}}^2-5\right)\cosh^{-1}(r_{\mathrm{a}})\Big).\end{aligned} \tag{4.27}$$

4.3 Simplification of the results

Figure 4.1 shows the dependence of the viscosity parameters $\bar{\eta}/\eta_{\mathrm{m}}, \bar{N}_{\mathrm{s}}, \bar{N}_{\mathrm{p}}$ on the fiber volume fraction $\bar{c}_{\mathrm{f}}$ and on the aspect ratio r_{a} (equations (4.25)-(4.27)) over a range of $\bar{c}_{\mathrm{f}} \in (0, 0.8)$ and $r_{\mathrm{a}} \in (30, 300)$. The considered aspect ratio range is typical for fiber suspensions in engineering applications, while the commonly used highest fiber volume fraction in the case of injection molding is about 30% (see, e.g., Fu et al. (2000)).

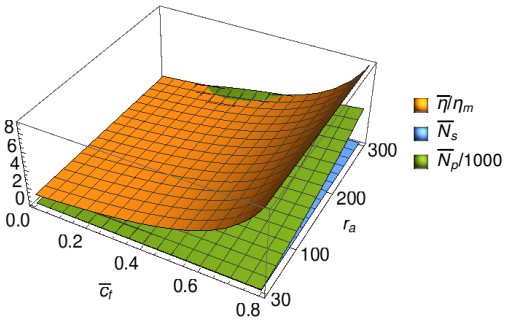

Figure 4.1: The relative effective scalar viscosity $\bar{\eta}/\eta_\mathrm{m}$, the shear number $\bar{N}_\mathrm{s}$ and the scaled particle number $\bar{N}_\mathrm{p}/1000$ as functions of the fiber volume fraction $\bar{c}_\mathrm{f}$ and the aspect ratio r_a, predicted by Mori-Tanaka's method.

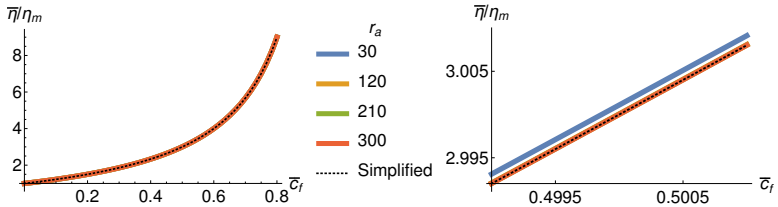

Figure 4.2: The relative effective scalar viscosity $\bar{\eta}/\eta_\mathrm{m}$ vs. the fiber volume fraction $\bar{c}_\mathrm{f}$ for different length to diameter aspect ratios r_a (left) and the same magnified around $\bar{c}_\mathrm{f} = 0.5$ (right) to show the slight dependence on r_a. The dashed line depicts the simplified model.

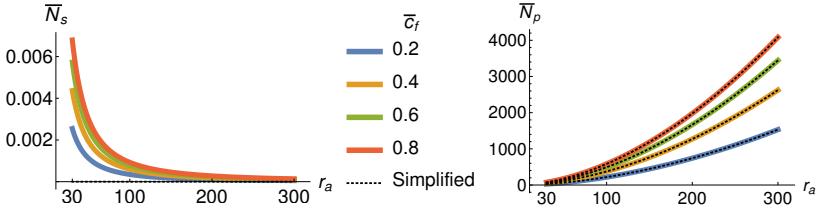

Figure 4.3: The shear number $\bar{N}_\mathrm{s}$ (left) and the particle number $\bar{N}_\mathrm{p}$ (right) vs. the fiber length to diameter aspect ratios r_a for different fiber volume fraction $\bar{c}_\mathrm{f}$. The dashed line depicts the simplified model.

Based on Figure 4.1, the following intuitive qualitative simplifications are introduced:

$$\bar{\eta} = \bar{\eta}(\bar{c}_\mathrm{f}), \tag{4.28}$$

$$\bar{N}_\mathrm{s} \approx 0, \tag{4.29}$$

$$\bar{N}_\mathrm{p} = \bar{N}_\mathrm{p}(r_\mathrm{a}, \bar{c}_\mathrm{f}), \tag{4.30}$$

where equation (4.28) notes the assumption that $\bar{\eta}$ depends solely on $\bar{c}_\mathrm{f}$. In the case of rigid fibers, with large aspect ratio: $r_\mathrm{a} \gg 1$, the approximations

$$r_\mathrm{a}^2 \pm i \approx r_\mathrm{a}^2 \quad \text{for } |i| \leq 2, \tag{4.31}$$

$$r_\mathrm{a}^{j+2} \pm \mathcal{O}(r_\mathrm{a}^j) \approx r_\mathrm{a}^{j+2} \quad \text{for } j \geq 0, \tag{4.32}$$

$$1/r_\mathrm{a}^k \approx 0 \quad \text{for } k \geq 2, \tag{4.33}$$

$$\cosh^{-1}(r_\mathrm{a}) = \ln(r_\mathrm{a} + \sqrt{r_\mathrm{a}^2 - 1}) \approx \ln(2r_\mathrm{a}) \tag{4.34}$$

appear reasonable for engineering applications. With these approximations, (4.25)-(4.27) result in

$$\bar{\eta} \approx \eta_\mathrm{m} \frac{1 + \bar{c}_\mathrm{f}}{1 - \bar{c}_\mathrm{f}}, \tag{4.35}$$

$$\bar{N}_\mathrm{s} \approx 0, \tag{4.36}$$

$$\bar{N}_\mathrm{p} \approx \frac{\bar{c}_\mathrm{f}}{1 + \bar{c}_\mathrm{f}} \frac{r_\mathrm{a}^2}{2(\ln(2r_\mathrm{a}) - 3/2)}. \tag{4.37}$$

Figures 4.2-4.3 show that the difference between the original and the simplified model is minimal, taking into account that the parameters $\bar{N}_s$ and $\bar{N}_p$ are linearly combined to get $\bar{\mathbb{V}}$ – see equation (2.12) – and $\bar{N}_s$ is at least three orders of magnitude smaller than $\bar{N}_p$, see Figure 4.1. This is the reason for setting the value of $\bar{N}_s$ to constant zero.

With the simplifications (4.35)-(4.37), equation (2.12) reduces to

$$\bar{\mathbb{V}}^{\mathrm{mf}}(\bar{\eta}, \bar{N}_{\mathrm{p}}, \bar{\mathbb{N}}) = 2\bar{\eta}\Bigg(\mathbb{P}_2 + \bar{N}_{\mathrm{p}}\left(\bar{\mathbb{N}} - \frac{1}{3}\left(\mathbf{1}\otimes\bar{\boldsymbol{N}} + \bar{\boldsymbol{N}}\otimes\mathbf{1}\right) + \frac{1}{9}\left(\mathbf{1}\otimes\mathbf{1}\right)\right)\Bigg) \tag{4.38}$$

which is analogous to the two-parameter-form of the effective viscosity, also used by, e.g., Latz et al. (2010). We denote by $\bar{\mathbb{V}}^{\mathrm{mf}}$ the simplified form (4.38) of (2.12), due to the fact, that the simplifications are the results of evaluating the mean-field theory.

In the next chapter, numerical full-field simulations, i.e., numerical experiments, are considered to evaluate the accuracy of the theoretically predicted values of the viscosity parameters (4.35)-(4.37). Furthermore, the validity of (2.12) and its simplified form (4.38) – both of them approximating the effective viscosity $\bar{\mathbb{V}}$ – are investigated.

Chapter 5

Full-field homogenization of viscous properties

5.1 Preliminaries

5.1.1 Synthetic microstructures

For the numerical full-field homogenization, single fiber geometries and numerically generated, so-called synthetic, microstructures are used, generated by an algorithm of Schneider (2017) using the exact closure method of Montgomery-Smith et al. (2011a). Periodic boundary conditions are applied in all cases and the microstuctures are voxelized, i.e., spatially discretized on a regular grid, for the numerical full-field homogenization. Figure 5.1 shows examples for unidirectional (ud), planar isotropic (piso), isotropic (iso) and a frequently occurring (7715) (Köbler et al., 2018) fiber-orientation state, corresponding to the second-order fiber-orientation tensors

$$\bar{\boldsymbol{N}}_{\text{ud}} \mathrel{\widehat{=}} \text{diag}(1,0,0), \qquad \bar{\boldsymbol{N}}_{\text{piso}} \mathrel{\widehat{=}} \text{diag}(0.5,0.5,0),$$
$$\bar{\boldsymbol{N}}_{\text{iso}} \mathrel{\widehat{=}} \text{diag}(0.33,0.33,0.33), \qquad \bar{\boldsymbol{N}}_{7715} \mathrel{\widehat{=}} \text{diag}(0.77,0.15,0),$$

respectively.

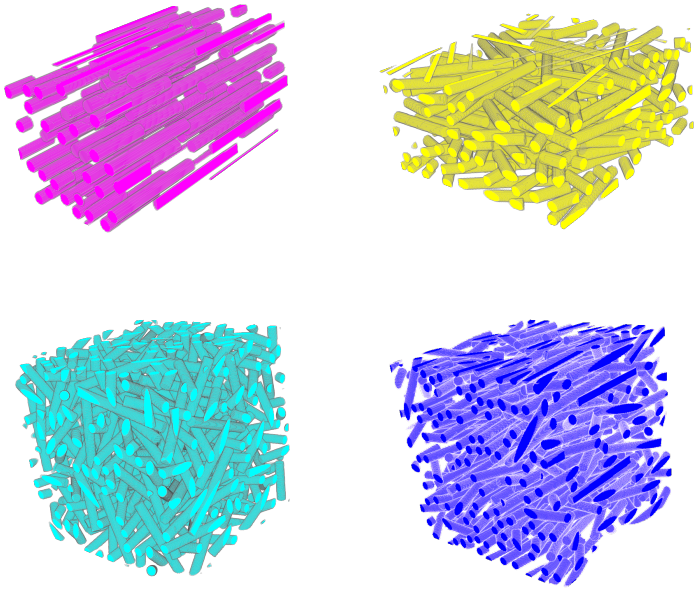

Figure 5.1: Examples of synthetic microstructures, from left to right and top to bottom: unidirectional (magenta), planar isotropic (yellow), isotropic (cyan) and a frequently occurring (Köbler et al. (2018), blue) fiber-orientation state, corresponding to the second-order fiber-orientation tensors depicted in equations above.

5.1.2 Computational setup and used hardware

The numerical homogenization of the viscosity, based on the synthetic microstructure data, is carried out by using the homKIT package developed by Matti Schneider et al. at the Institute of Engineering Mechanics, Karlsruhe Institute of Technology (KIT) based on Schneider et al. (2016). For the computations a dual framework (Schneider, 2016) and the Barzilai-Borwein solver (Barzilai and Borwein, 1988; Schneider, 2019; Wicht et al., 2020) are used. The fibers are assumed to be rigid, therefore, the velocity gradient within the fibers is constant zero, see Figure 5.2.

The computed stress within the fibers is not constant, see Figure 5.3, this is the main difference in contrast to the mean-field model.

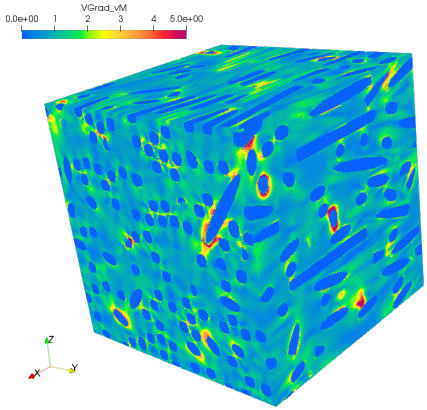

Figure 5.2: Example of the computed velocity gradient field, considering a shear flow.

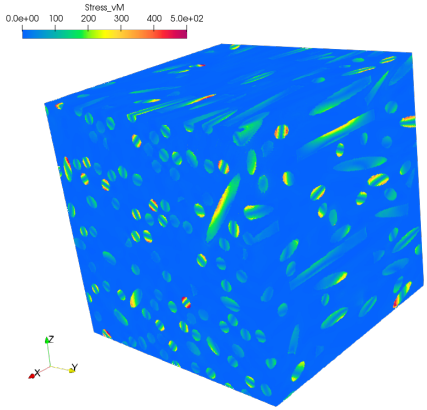

Figure 5.3: Example of the computed stress field, considering a shear flow.

The computations are carried out using a computer with 8 GB RAM and 3.50GHz×4 CPU.

5.1.3 Fast approximation of the viscosity parameters in the case of aligned fibers

In the case of unidirectionally aligned fibers ($\boldsymbol{n}_{\mathrm{ud}} \widehat{=} (1,0,0)$), the second- and the fourth-order orientation tensors are exactly described by

$$\bar{\boldsymbol{N}}_{\mathrm{ud}} \widehat{=} \begin{pmatrix} 1 & 0 & 0 \\ 0 & 0 & 0 \\ 0 & 0 & 0 \end{pmatrix} \text{ and } \bar{\mathbb{N}}_{\mathrm{ud}} = \bar{\boldsymbol{N}}_{\mathrm{ud}} \otimes \bar{\boldsymbol{N}}_{\mathrm{ud}} \widehat{=} \begin{pmatrix} 1 & 0 & 0 & 0 & 0 & 0 \\ 0 & 0 & 0 & 0 & 0 & 0 \\ 0 & 0 & 0 & 0 & 0 & 0 \\ 0 & 0 & 0 & 0 & 0 & 0 \\ 0 & 0 & 0 & 0 & 0 & 0 \\ 0 & 0 & 0 & 0 & 0 & 0 \end{pmatrix}, \tag{5.1}$$

where the first axis is directed parallel to the fiber direction and the other two perpendicular to the fiber. By using these orientation tensors and the general form of the viscosity tensor (2.12), the deviatoric effective stress tensor for unidirectional fibers $\bar{\boldsymbol{\sigma}}'_{\mathrm{ud}} = \bar{\mathbb{V}}_{\mathrm{ud}}[\bar{\boldsymbol{D}}']$ results in the form

$$\bar{\boldsymbol{\sigma}}'_{\mathrm{ud}}(\bar{\boldsymbol{D}}') = 2\bar{\eta} \left(\bar{\boldsymbol{D}}' + \bar{N}_{\mathrm{s}} \begin{pmatrix} \frac{4}{3}\bar{D}'_{11} & \bar{D}'_{12} & \bar{D}'_{13} \\ \bar{D}'_{12} & -\frac{2}{3}\bar{D}'_{11} & 0 \\ \bar{D}'_{13} & 0 & -\frac{2}{3}\bar{D}'_{11} \end{pmatrix} + \bar{N}_{\mathrm{p}} \begin{pmatrix} \frac{2}{3}\bar{D}'_{11} & 0 & 0 \\ 0 & -\frac{1}{3}\bar{D}'_{11} & 0 \\ 0 & 0 & -\frac{1}{3}\bar{D}'_{11} \end{pmatrix} \right). \tag{5.2}$$

With three special deformation rates, namely

$$\bar{\boldsymbol{D}}^{(\bar{\eta})} \;\hat{=}\; \begin{pmatrix} 0 & 0 & 0 \\ 0 & 0 & 1 \\ 0 & 1 & 0 \end{pmatrix}, \tag{5.3}$$

$$\bar{\boldsymbol{D}}^{(\bar{N}_\mathrm{s})} \;\hat{=}\; \begin{pmatrix} 0 & 1 & 0 \\ 1 & 0 & 0 \\ 0 & 0 & 0 \end{pmatrix}, \tag{5.4}$$

$$\bar{\boldsymbol{D}}^{(\bar{N}_\mathrm{p})} \;\hat{=}\; \begin{pmatrix} 1 & 0 & 0 \\ 0 & -1 & 0 \\ 0 & 0 & 0 \end{pmatrix}, \tag{5.5}$$

the viscosity parameters can be approximated easily and quickly, i.e., with only one load case per unknown viscosity parameter. The formulas to identify the viscosity parameters read

$$\bar{\boldsymbol{\sigma}}_{\mathrm{ud}}^{(\bar{\eta})} \cdot \bar{\boldsymbol{D}}^{(\bar{\eta})} = 4\bar{\eta}, \tag{5.6}$$

$$\bar{\boldsymbol{\sigma}}_{\mathrm{ud}}^{(\bar{N}_\mathrm{s})} \cdot \bar{\boldsymbol{D}}^{(\bar{N}_\mathrm{s})} = 4(1+\bar{N}_\mathrm{s})\bar{\eta}, \tag{5.7}$$

$$\bar{\boldsymbol{\sigma}}_{\mathrm{ud}}^{(\bar{N}_\mathrm{p})} \cdot \bar{\boldsymbol{D}}^{(\bar{N}_\mathrm{p})} = 2\bar{\eta}(2+2\bar{N}_\mathrm{s}+\bar{N}_\mathrm{p}), \tag{5.8}$$

where the stress tensors $\bar{\boldsymbol{\sigma}}_{\mathrm{ud}}^{(\bar{\eta})}, \bar{\boldsymbol{\sigma}}_{\mathrm{ud}}^{(\bar{N}_\mathrm{s})}, \bar{\boldsymbol{\sigma}}_{\mathrm{ud}}^{(\bar{N}_\mathrm{p})}$, corresponding to the strain rates $\bar{\boldsymbol{D}}^{(\bar{\eta})}, \bar{\boldsymbol{D}}^{(\bar{N}_\mathrm{s})}, \bar{\boldsymbol{D}}^{(\bar{N}_\mathrm{p})}$, are computed by homKIT numerically. Recall that the symbol $\cdot$ denotes the scalar product.

The results in the subsections 5.1.4-5.1.6 are computed with the above described fast approximation. The numerical determination of the complete viscosity tensor and the corresponding viscosity parameters – in a least-squares manner – is described in section 5.2.

5.1.4 Resolution study

The numerical results and the computation times depend strongly on the voxel-resolution of the fibers and of the volume element. Therefore, the optimal resolution of a single fiber was investigated, considering the effective stress in fiber direction $\bar{\sigma}_{xx}$, the effective scalar viscosity $\bar{\eta}$, the shear number $\bar{N}_\mathrm{s}$ and the particle number $\bar{N}_\mathrm{p}$. The investigated resolutions and the results are depicted in Figures 5.4 and 5.5, respectively.

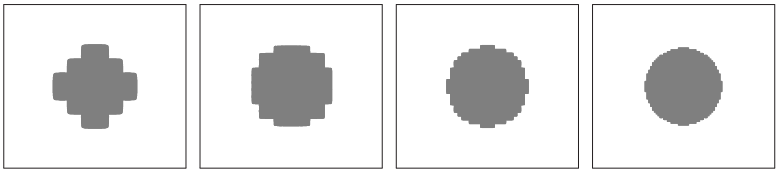

Figure 5.4: Investigated resolutions, left to right: 5, 10, 20 and 40 voxels/fiber diameter.

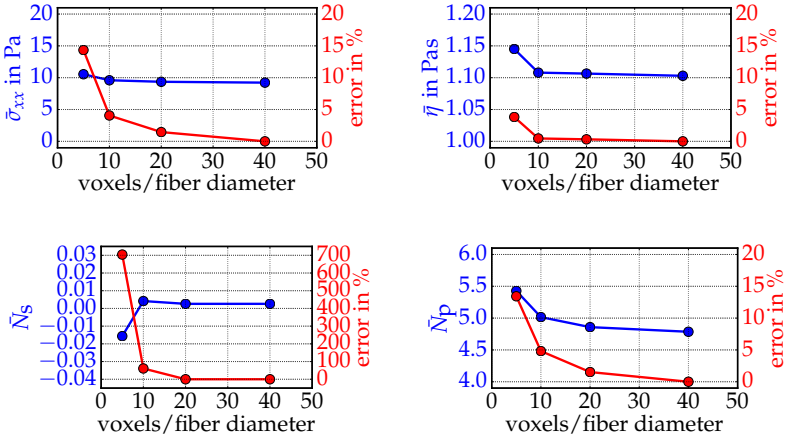

Figure 5.5: Resolution dependence of $\bar{\sigma}_{xx}$, $\bar{\eta}$, $\bar{N}_\mathrm{s}$ and $\bar{N}_\mathrm{p}$, for $r_\mathrm{a} = 10, \bar{c}_\mathrm{f} = 5\%$.

Over 10 voxels/fiber diameter, the errors, relative to the results of the highest resolution (40 voxels/fiber diameter) are below 5% except for $\bar{N}_\mathrm{s}$, whose value is almost zero. Based on these results all further computations are carried out with resolution of 12 voxels/fiber diameter.

5.1.5 Microstructure dependence of the viscosity parameters

The mean-field model-results, cf. equations (4.35)-(4.37), describe the dependence of the viscosity parameters $\bar{\eta}$, $\bar{N}_\mathrm{s}$ and $\bar{N}_\mathrm{p}$ on the material and microstructure parameters η_m (matrix viscosity), $\bar{c}_\mathrm{f}$ (fiber volume fraction) and $r_\mathrm{a} = l/d$ (fiber aspect ratio). The mean-field model assumes that a representative volume element is considered. However, a single fiber in a periodic cell is not representative for distributed fibers, but such a simple microstructure allows a quick qualitative comparison of the mean-field and the full-field methods considering the microstructure dependence of the viscosity parameters, see Figs. 5.6-5.8 with detailed explanation in their captions.

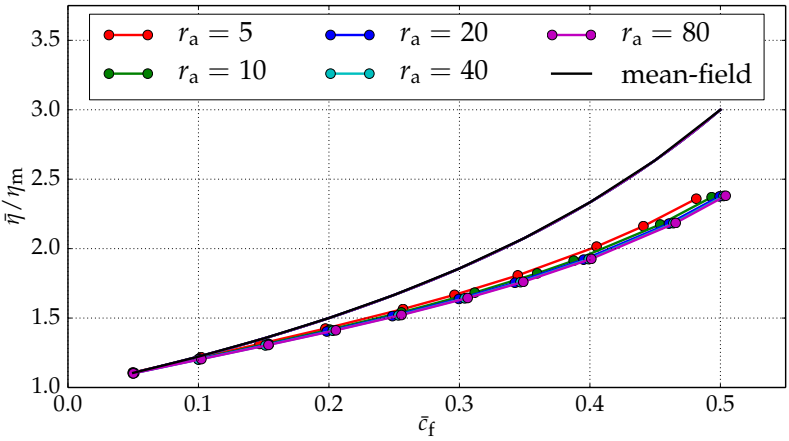

Figure 5.6: Microstructure dependence of the effective viscosity $\bar{\eta}$ relative to the matrix viscosity η_m vs. the fiber volume fraction $\bar{c}_\mathrm{f}$, for different aspect ratios $r_\mathrm{a} = l/d$. The colored lines with the markers are the results of the full-field model considering one single fiber in the volume element with periodic boundary conditions. The black line is the prediction of the mean-field model corresponding to a representative volume element. The mean-field homogenization predicted that $\bar{\eta}$ is independent of r_a. This independence is confirmed by the full-field model. Beside the qualitative similarity of the two models a quantitative difference is specified in the considered cases.

Figure 5.6 depicts the microstructure dependence of the effective viscosity $\bar{\eta}$ relative to the matrix viscosity η_m over the fiber volume fraction $\bar{c}_\mathrm{f}$, considering different r_a aspect ratios. The independence of $\bar{\eta}$ from r_a, predicted by the mean-field homogenization, is confirmed by the full-field model. Beside the qualitative similarity of the two models, a quantitative difference is specified in the considered cases. The quantitative difference could be caused by considering only one single fiber in the periodic cell of the full-field model, which is not representative – contrary to the assumption of the mean-field model – for unidirectionally distributed fibers.

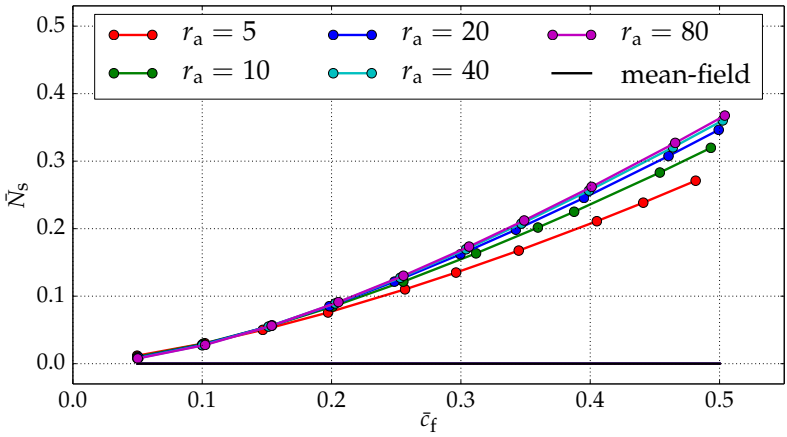

Figure 5.7: Microstructure dependence of the shear number $\bar{N}_\mathrm{s}$ on the fiber volume fraction $\bar{c}_\mathrm{f}$, for different aspect ratios $r_\mathrm{a} = l/d$. The colored lines with the markers are the results of the full-field model considering one single fiber in the volume element with periodic boundary conditions. The black horizontal line is the prediction of the mean-field model corresponding to a representative volume element. Neglecting the shear number ($\bar{N}_\mathrm{s} = 0$), as predicted by the mean-field homogenization, is justified by full-field model only relative to $\bar{\eta}$ and $\bar{N}_\mathrm{p}$.

The microstructure dependence of the shear number $\bar{N}_\mathrm{s}$ on the fiber volume fraction $\bar{c}_\mathrm{f}$, considering different r_a aspect ratios, is shown in Figure 5.7. The magnitude of $\bar{N}_\mathrm{s}$ is, for all investigated cases, at least one order smaller than the corresponding $\bar{\eta}$ and $\bar{N}_\mathrm{p}$ values. This justifies

to neglect the shear number ($\bar{N}_\mathrm{s} = 0$), as predicted by the mean-field homogenization.

Figure 5.8 depicts the microstructure dependence of the particle number $\bar{N}_\mathrm{p}$ on the fiber volume fraction $\bar{c}_\mathrm{f}$, considering different aspect ratios r_a. Beside the qualitative similarity of the two models, a quantitative difference is observed.

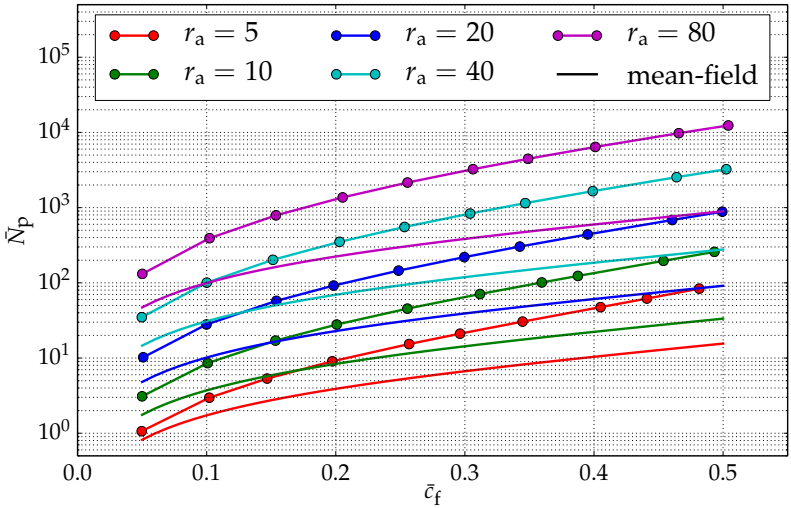

Figure 5.8: Microstructure dependence of the particle number $\bar{N}_\mathrm{p}$ over the fiber volume fraction $\bar{c}_\mathrm{f}$, for different fiber length to fiber diameter aspect ratios $r_\mathrm{a} = l/d$. The colored lines with the markers are the results of the full-field model considering one single fiber in the volume element with periodic boundary conditions. The colored lines without the markers are the predictions of the mean-field model corresponding to representative volume elements. Note that the vertical axis has a logarithmic scale.

Based on the considered 50 different single fiber microstuctures and the corresponding 150 computations it can be stated that the "single fiber model", i.e., the full-field model of one single fiber in the volume element with periodic boundary conditions, gives qualitatively the same results as the mean-field model, but quantitatively they are different. The results

of the mean-field model are gained assuming a representative volume element of *randomly* distributed fibers. This assumption is not fulfilled by the "single fiber model" which could be the reason for the quantitative difference of the mean-field and the full-field models.

In the next sections the analysis is extended, examining several aligned fibers and the effect of the volume element size. In the following, fibers with aspect ratio $r_a = 10$ are investigated.

5.1.6 Estimation of the RVE size in the case of aligned fibers

One of the reasons for the difference between the mean-field and the full-field models in the Figures 5.6 and 5.8 could be that one single fiber and the surrounding matrix material with periodic boundary conditions is not a representative volume element. To investigate the representativity of volume elements, synthetic microstructures are generated, for further details see section 5.1.1.

In this subsection, only aligned synthetic microstructures are considered, and square-column shaped ($L \times W \times W$) volume elements of different sizes are randomly filled with unidirectionally aligned fibers. The length L and the width W of the volume elements are varied relative to the fiber length l and the fiber diameter d, respectively, as shown in the Figures 5.9 and 5.11.

The mean values and the scatter of the resulting effective viscosities are compared for the different volume element sizes. A volume element is considered to be representative, if a larger volume element does result in almost the same mean value and scatter of the effective viscosity (Gitman et al., 2007). The results for varying the volume element length and the volume element width are depicted in Figure 5.10 and Figure 5.12, respectively.

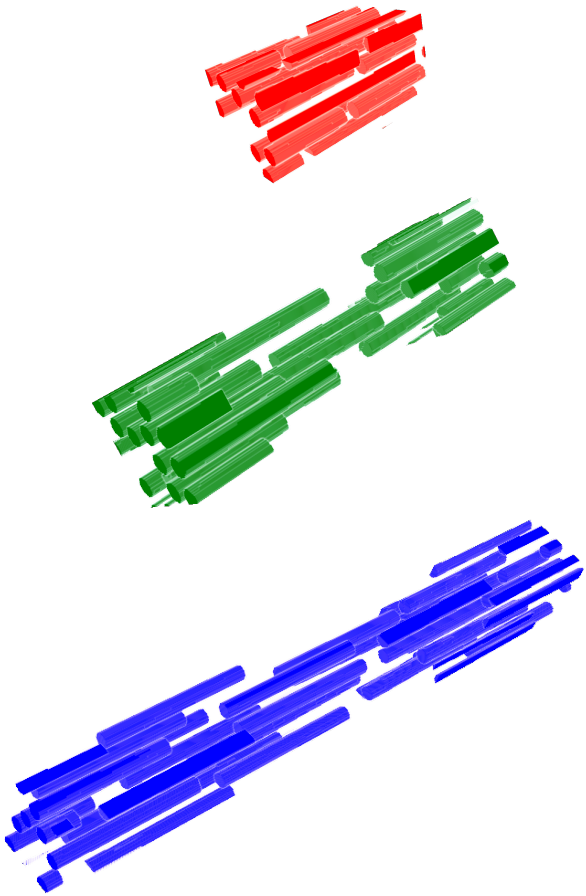

Figure 5.9: Axonometric view of unidirectional synthetic microstructures, in square-column shaped ($L \times W \times W$) volume elements of different sizes (from top to bottom): $L = 1.1l$, $L = 2.2l$, and $L = 4.4l$, where l is the fiber length and L the volume element length. The volume element width is set to $W = 5d$ in each case, where d denotes the fiber diameter.

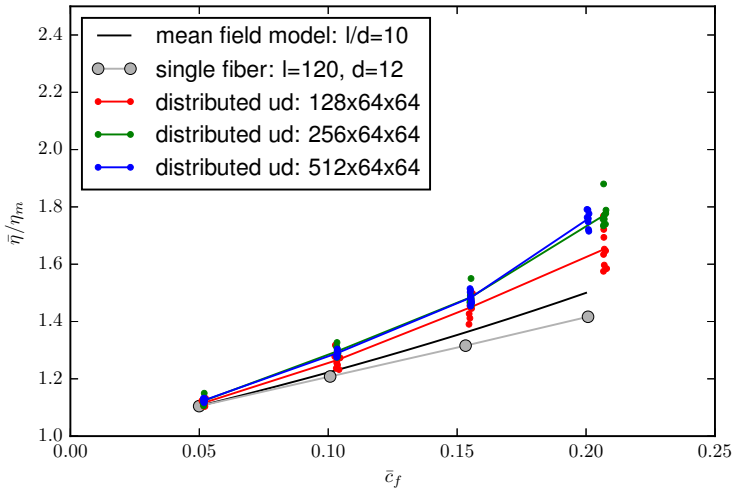

Figure 5.10: RVE study: varying the volume element length in voxels.

The curves in Figure 5.10 shows the mean value and the scatter of the relative effective viscosity vs. the fiber volume fraction for different lengths of a volume element, according to the microstructures and the color code of Figure 5.9. For each volume element length and for each fiber volume fraction eight randomly filled unidirectional microstructures are investigated, leading to the scatter in the diagram. The continuous lines connect the mean values. The results of one single fiber in a periodic volume element are also depicted in the figure with grey.

Volume elements with the length $L = 2.2l$ (green curve) give the same mean values as the case $L = 4.4l$ (blue curve), and the difference in their scatter is negligible for engineering purposes. The problem of the volume elements with lengths $L = 1.1l$ (red curve) is that the distance between two fiber ends is always $0.1l$. This unrealistic condition cannot occure for volume element lengths exceeding $L = 2l$. Based on these investigations, the volume element length $L = 2.2l$ is considered to be representative for microstructures of aligned fibers.

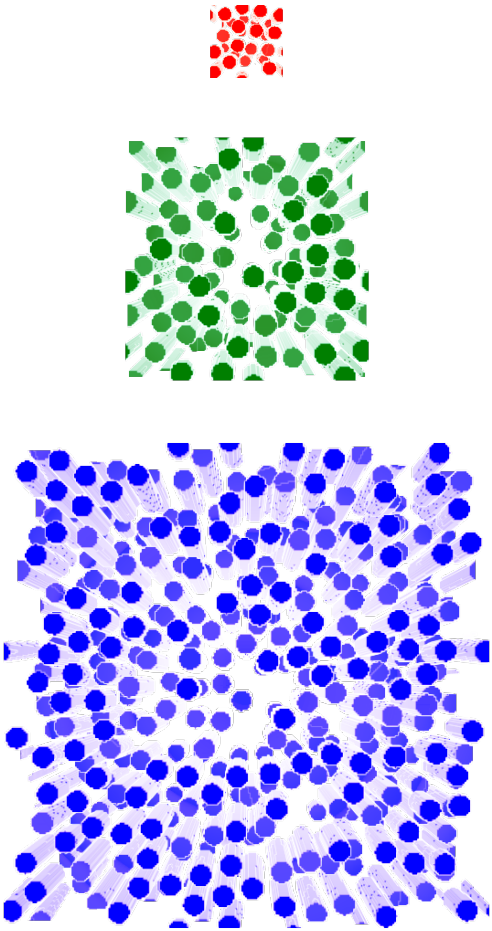

Figure 5.11: Front view of unidirectional synthetic microstructures, in square-column shaped ($L \times W \times W$) volume elements of different sizes (from top to bottom): $W = 5d$, $W = 10d$ and $W = 20d$, where d is the fiber diameter and W the volume element width. The volume element length is set to $L = 2.2l$ in each case, where l denotes the fiber length.

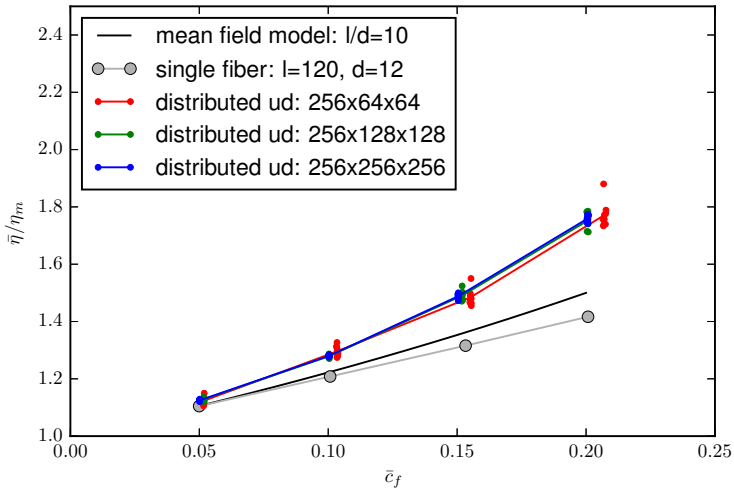

Figure 5.12: RVE study: varying the volume element width in voxels.

Figure 5.12 shows the mean value and the scatter of the relative effective viscosity vs. the fiber volume fraction, considering different widths of a volume element according to the microstructures and the color code of Figure 5.11. For each volume element width and for each fiber volume fraction, eight randomly filled unidirectional microstructures are investigated, inducing the scatter in the diagram. The continuous lines connect the mean values. The results of one single fiber in a periodic volume element are also included in the figure.

The mean values are almost the same in all of the three considered cases, but the scatter for $W = 10d$ and above (green and blue colors in the diagram) is smaller than the scatter in the case of the smallest investigated volume element width, i.e., $W = 5d$ (red color in the diagram). Based on these investigations, the volume element width $W = 10d$ is considered as representative volume element width for microstructures of aligned fibers.

From now on $\eta_\mathrm{m} = 1$ Pas is used and only $\bar{\eta}$ is referred instead of $\bar{\eta}/\eta_\mathrm{m}$, because the effective viscosity $\bar{\mathbb{V}}$ is linear in η_m.

5.2 Determination of the effective viscosity

5.2.1 Assumptions on the RVE size

Besides aligned fibers (ud), three cases of non-aligned fibers are investigated: planar isotropic (piso), isotropic (iso), and a common (7715) – i.e., frequently occurring (Köbler et al., 2018), not transversely isotropic – fiber-orientation state, with fiber-orientation tensors

$$\bar{\boldsymbol{N}}_\mathrm{ud} \;\widehat{=}\; \mathrm{diag}(1,0,0), \tag{5.9}$$

$$\bar{\boldsymbol{N}}_\mathrm{piso} \;\widehat{=}\; \mathrm{diag}(0.5,0.5,0), \tag{5.10}$$

$$\bar{\boldsymbol{N}}_\mathrm{iso} \;\widehat{=}\; \mathrm{diag}(0.33,0.33,0.33), \tag{5.11}$$

$$\bar{\boldsymbol{N}}_{7715} \;\widehat{=}\; \mathrm{diag}(0.77,0.15,0), \tag{5.12}$$

respectively, see Figure 5.1 for examples. The considered volume element sizes – for each orientation state separately – are chosen based on the results of the former subsection 5.1.6. For the unidirectional cases, square-column shaped volume elements of the size $L \times W \times W$ are considered. For the planar isotropic cases, also square-column shaped volume elements, but of the size $L \times L \times W$ are used. For the isotropic and the frequently occurring cases, cubic $L \times L \times L$ sized volume elements are considered. The volume elements with $L = 2.2l$ and $W = 20d$ are assumed to be representative, where l denotes the fiber length and d the fiber diameter. This assumption is confirmed by the acceptable scatter of the results – regarding the viscosity parameters $\bar{\eta},\ \bar{N}_\mathrm{s},$ and $\bar{N}_\mathrm{p}$ – in all investigated cases, see the scatter in the diagrams of the subsections 5.3-6.3.

5.2.2 Numerical determination of the effective viscosity

The numerical approximation $\bar{\mathbb{V}}^{\mathrm{num}}$ of the effective viscosity tensor $\bar{\mathbb{V}}$ is determined through computing the deviatoric effective stress response of the synthetic microstuctures according to the following six effective load cases:

$$\bar{\boldsymbol{D}}^{(1)} \hat{=} \begin{pmatrix} 1 & 0 & 0 \\ 0 & 1 & 0 \\ 0 & 0 & 1 \end{pmatrix}, \quad \bar{\boldsymbol{D}}^{(2)} \hat{=} \begin{pmatrix} 1 & 0 & 0 \\ 0 & -1 & 0 \\ 0 & 0 & 0 \end{pmatrix},$$

$$\bar{\boldsymbol{D}}^{(3)} \hat{=} \begin{pmatrix} 0 & 0 & 0 \\ 0 & 1 & 0 \\ 0 & 0 & -1 \end{pmatrix}, \quad \bar{\boldsymbol{D}}^{(4)} \hat{=} \begin{pmatrix} 0 & 0 & 0 \\ 0 & 0 & 1 \\ 0 & 1 & 0 \end{pmatrix}, \tag{5.13}$$

$$\bar{\boldsymbol{D}}^{(5)} \hat{=} \begin{pmatrix} 0 & 0 & 1 \\ 0 & 0 & 0 \\ 1 & 0 & 0 \end{pmatrix}, \quad \bar{\boldsymbol{D}}^{(6)} \hat{=} \begin{pmatrix} 0 & 1 & 0 \\ 1 & 0 & 0 \\ 0 & 0 & 0 \end{pmatrix}.$$

The deviatoric effective stress response $\bar{\boldsymbol{\sigma}}^{(1)}$ corresponding to $\bar{\boldsymbol{D}}^{(1)}$ must be zero, because $\bar{\boldsymbol{D}}^{(1)}$ is a spherical (hydrostatic) effective load case, which induces only spherical (hydrostatic) effective stresses, which do not enter $\bar{\mathbb{V}}'$ (see subsection 2.1.3, especially equations (2.6) and (2.9)). For the effective load cases $\bar{\boldsymbol{D}}^{(2)}$ to $\bar{\boldsymbol{D}}^{(6)}$, the deviatoric effective stresses $\bar{\boldsymbol{\sigma}}^{(i)}, i = 2, \ldots, 6$ are computed by homKIT, and they define the

numerical effective viscosity tensor in Mandel's notation (Mandel, 1965):

$$\begin{bmatrix} 0 & \bar{\sigma}_{11}^{(2)} & \bar{\sigma}_{11}^{(3)} & \bar{\sigma}_{11}^{(4)} & \bar{\sigma}_{11}^{(5)} & \bar{\sigma}_{11}^{(6)} \\ 0 & \bar{\sigma}_{22}^{(2)} & \bar{\sigma}_{22}^{(3)} & \bar{\sigma}_{22}^{(4)} & \bar{\sigma}_{22}^{(5)} & \bar{\sigma}_{22}^{(6)} \\ 0 & \bar{\sigma}_{33}^{(2)} & \bar{\sigma}_{33}^{(3)} & \bar{\sigma}_{33}^{(4)} & \bar{\sigma}_{33}^{(5)} & \bar{\sigma}_{33}^{(6)} \\ 0 & \sqrt{2}\bar{\sigma}_{23}^{(2)} & \sqrt{2}\bar{\sigma}_{23}^{(3)} & \sqrt{2}\bar{\sigma}_{23}^{(4)} & \sqrt{2}\bar{\sigma}_{23}^{(5)} & \sqrt{2}\bar{\sigma}_{23}^{(6)} \\ 0 & \sqrt{2}\bar{\sigma}_{13}^{(2)} & \sqrt{2}\bar{\sigma}_{13}^{(3)} & \sqrt{2}\bar{\sigma}_{13}^{(4)} & \sqrt{2}\bar{\sigma}_{13}^{(5)} & \sqrt{2}\bar{\sigma}_{13}^{(6)} \\ 0 & \sqrt{2}\bar{\sigma}_{12}^{(2)} & \sqrt{2}\bar{\sigma}_{12}^{(3)} & \sqrt{2}\bar{\sigma}_{12}^{(4)} & \sqrt{2}\bar{\sigma}_{12}^{(5)} & \sqrt{2}\bar{\sigma}_{12}^{(6)} \end{bmatrix} =$$

$$\begin{bmatrix} \bar{V}_{11} & \bar{V}_{12} & \bar{V}_{13} & \bar{V}_{14} & \bar{V}_{15} & \bar{V}_{16} \\ & \bar{V}_{22} & \bar{V}_{23} & \bar{V}_{24} & \bar{V}_{25} & \bar{V}_{26} \\ & & \bar{V}_{33} & \bar{V}_{34} & \bar{V}_{35} & \bar{V}_{36} \\ & & & \bar{V}_{44} & \bar{V}_{45} & \bar{V}_{46} \\ & \text{sym.} & & & \bar{V}_{55} & \bar{V}_{56} \\ & & & & & \bar{V}_{66} \end{bmatrix} \begin{bmatrix} 1 & 1 & 0 & 0 & 0 & 0 \\ 1 & -1 & 1 & 0 & 0 & 0 \\ 1 & 0 & -1 & 0 & 0 & 0 \\ 0 & 0 & 0 & \sqrt{2} & 0 & 0 \\ 0 & 0 & 0 & 0 & \sqrt{2} & 0 \\ 0 & 0 & 0 & 0 & 0 & \sqrt{2} \end{bmatrix}. \tag{5.14}$$

The matrix equation (5.14) is written in a short form as $\underline{\underline{\bar{\sigma}}} = \underline{\underline{\bar{V}}}\ \underline{\underline{\bar{D}}}$ from which it follows that $\underline{\underline{\bar{V}}} = \underline{\underline{\bar{\sigma}}}\ \underline{\underline{\bar{D}}}^{-1}$. Note that $\underline{\underline{\bar{\sigma}}}$ is singular, but $\underline{\underline{\bar{D}}}$ and $\underline{\underline{\bar{D}}}^{-1}$ are non-singular matrices. The first row of $\underline{\underline{\bar{\sigma}}}$ is zero, because the considered anisotropic material model (2.9) determines only the deviatoric stress, as already mentioned above. The tensor of the numerically determided $\underline{\underline{\bar{V}}}$ matrix is denoted by $\bar{\mathbb{V}}^{\text{num}}$, and it is considered as reference solution.

5.2.3 Numerical determination of the viscosity parameters

Approximating $\bar{\mathbb{V}}^{\text{num}}$ by the form (2.12), the fitted viscosity tensor $\bar{\mathbb{V}}^{\text{fit}}$ is determined by minimizing the error in a least-squares manner, i.e.,

$$e^{\text{fit}} := \min_{\bar{\eta},\bar{N}_{\text{s}},\bar{N}_{\text{p}}} \frac{||\bar{\mathbb{V}}^{\text{fit}}(\bar{\eta},\bar{N}_{\text{s}},\bar{N}_{\text{p}}) - \bar{\mathbb{V}}^{\text{num}}||}{||\bar{\mathbb{V}}^{\text{num}}||}. \tag{5.15}$$

The error of the mean-field model $\bar{\mathbb{V}}^{\mathrm{mf}}$ (4.38) is defined analogously

$$e^{\mathrm{mf}} := \frac{||\bar{\mathbb{V}}^{\mathrm{mf}} - \bar{\mathbb{V}}^{\mathrm{num}}||}{||\bar{\mathbb{V}}^{\mathrm{num}}||}. \tag{5.16}$$

The results for different cases are presented in the following section.

5.3 Resulting viscosity parameters considering different cases

5.3.1 Single fiber

The fitted viscosity parameters $\bar{\eta}, \bar{N}_{\mathrm{s}}, \bar{N}_{\mathrm{p}}$ and the error e for a single fiber (sf) are depicted in Figure 5.13. The error $e^{\mathrm{fit}}_{\mathrm{sf}} < 5\%$ is much smaller than the error $e^{\mathrm{mf}}_{\mathrm{sf}} < 75\%$, because of the large difference regarding $\bar{N}_{\mathrm{p}}$.

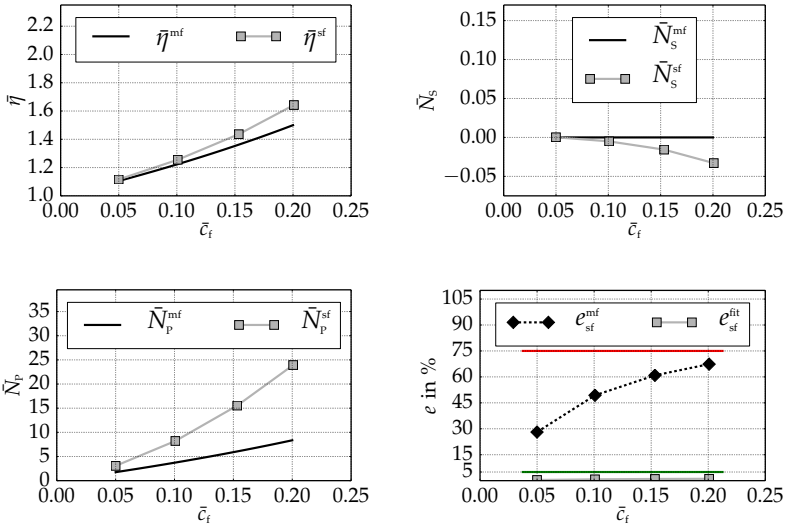

Figure 5.13: Mean-field (black) vs. fitted (grey) viscosity parameters $\bar{\eta}, \bar{N}_{\mathrm{s}}, \bar{N}_{\mathrm{p}}$ and the error e considering a *single fiber* (sf). The red and the green lines mark the upper limits of e.

5.3.2 Unidirectional case

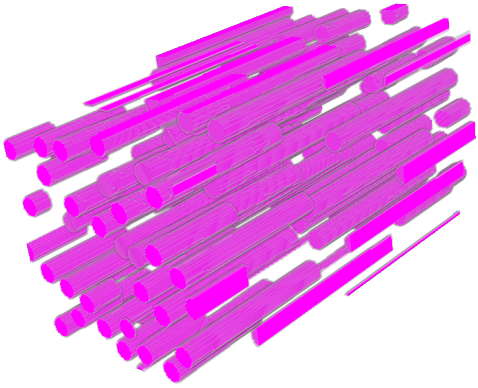

Figure 5.14: RVE of an *unidirectional* (ud) microstructure made up by straight fibers.

As expected – based on the subsections 5.1.5-5.1.6 – a single fiber in a periodic cell is not an RVE regarding randomly distributed unidirectional fibers. Considering the assumed representative volume element size: $L \times W \times W = 2.2l \times 10d \times 10d$ for unidirectionally aligned fibers (see for example Figure 5.14), the results are much closer to the mean-field predictions than they were in the case of the single fiber (see Figure 5.13 vs. Figure 5.15).

In the diagrams of Figure 5.15, the resulting fitted viscosity parameters $\bar{\eta}, \bar{N}_\mathrm{s}, \bar{N}_\mathrm{p}$, and the relative error of the fitted (e^fit) and of the mean-field (e^mf) model are shown in the case of unidirectional microstructures, for fiber volume fractions in the range of 5%-20%.

The fitted effective viscosity $\bar{\eta}^\mathrm{ud}$ is consistently higher than the effective viscosity $\bar{\eta}^\mathrm{mf}$ of the mean-field model. The scatter of $\bar{\eta}^\mathrm{ud}$ is smaller than the magenta disk shaped markers, this is the reason why the scatter is not visible. Note that $\bar{\eta}^\mathrm{ud}$ is slightly higher than $\bar{\eta}^\mathrm{sf}$.

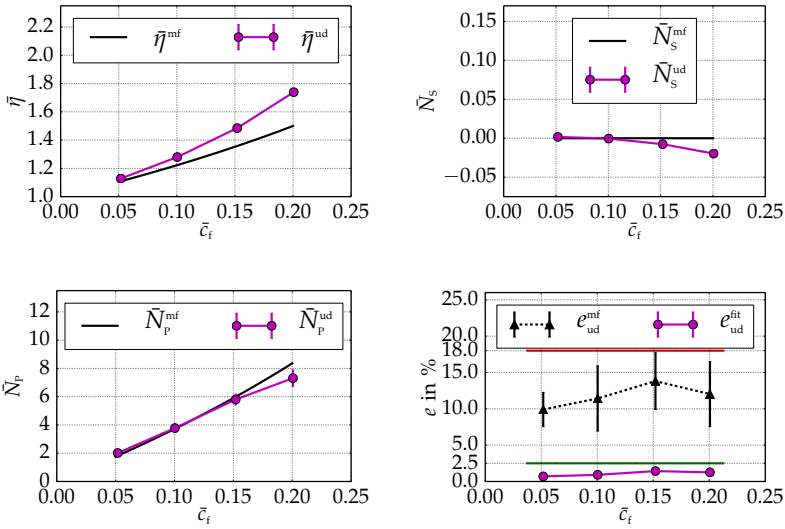

Figure 5.15: Mean-field (black) vs. fitted (magenta) viscosity parameters $\bar{\eta}$, $\bar{N}_s$, $\bar{N}_p$ and the error e considering the *unidirectional* (ud) fiber-orientation sate. The red and the green lines mark the upper limits of e.

The fitted effective shear number $\bar{N}_s^{ud}$ is in an average sense lower than the effective shear number $\bar{N}_s^{mf}$ of the mean-field model, but $\bar{N}_s^{ud}$ is very close to zero and to $\bar{N}_s^{sf}$. The scatter of $\bar{N}_s^{ud}$ cannot be seen.

The fitted effective particle number $\bar{N}_p^{ud}$ is almost identical to the effective particle number $\bar{N}_p^{mf}$ of the mean-field model, only for the highest investigated fiber volume fraction $\bar{c}_f = 20\%$ there exists a small difference. A small scatter of $\bar{N}_p^{ud}$ can be seen, but the magnitude of the scatter is small enough to consider the investigated volume element ($2.2l \times 10d \times 10d$) henceforth as an RVE. Note that $\bar{N}_p^{ud}$ is much closer to the mean-field predictions than $\bar{N}_p^{sf}$.

The error $e_{ud}^{fit} < 2.5\%$ is much smaller than the error $e_{ud}^{mf} < 18\%$, because of the difference in $\bar{\eta}$. The scatter of e_{ud}^{fit} is so small that it cannot be seen. Also note the difference between $e_{ud}^{fit} < 2.5\%$ and $e_{sf}^{fit} < 5\%$.

5.3.3 Planar isotropic case

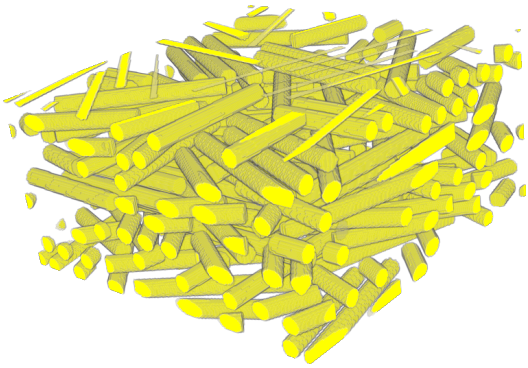

Figure 5.16: RVE of a *planar isotropic* (piso) microstructure made up by straight fibers.

Based on the estimations and the assumptions on the RVE (see sections 5.1.6 and 5.2.1), the size of the representative volume element for the planar isotropic case is considered to be: $L \times L \times W = 2.2l \times 2.2l \times 10d$, see for example Figure 5.16.

In the diagrams of Figure 5.17, the resulting fitted viscosity parameters $\bar{\eta}, \bar{N}_\mathrm{s}, \bar{N}_\mathrm{p}$, the relative error of the fitted (e^fit) and of the mean-field (e^mf) model are shown in the case of planar isotropic microstructures, for fiber volume fractions in the range of 5%-20%.

The fitted effective viscosity $\bar{\eta}^\mathrm{piso}$ is consistently higher than the effective viscosity $\bar{\eta}^\mathrm{mf}$ of the mean-field model. A small scatter of $\bar{\eta}^\mathrm{piso}$ can be seen, but the magnitude of the scatter is small enough to consider the investigated volume element ($2.2l \times 2.2l \times 10d$) henceforth as RVE.

The fitted effective shear number $\bar{N}_\mathrm{s}^\mathrm{piso}$ is slightly lower than the effective shear number $\bar{N}_\mathrm{s}^\mathrm{mf}$ of the mean-field model, but $\bar{N}_\mathrm{s}^\mathrm{piso}$ is very close to

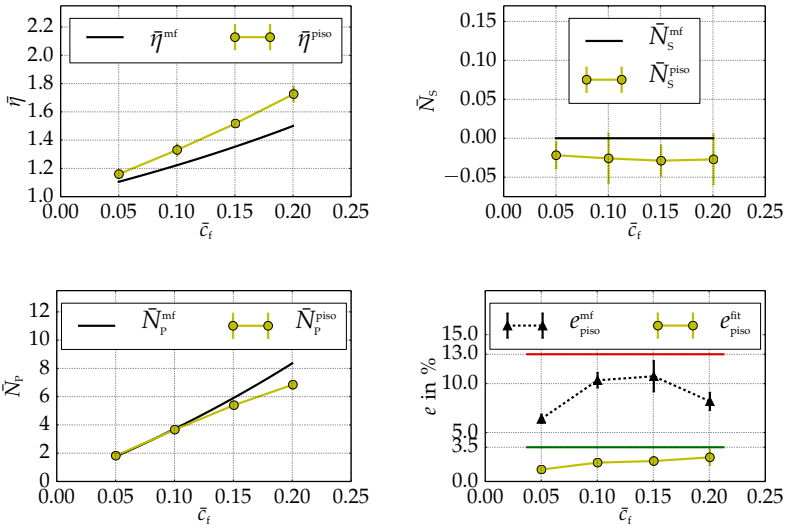

Figure 5.17: Mean-field (black) vs. fitted (yellow) viscosity parameters $\bar{\eta}$, $\bar{N}_{\mathrm{s}}$, $\bar{N}_{\mathrm{p}}$ and the error e considering the *planar isotropic* (piso) fiber-orientation state. The red and the green lines mark the upper limits of e.

zero. The maximum of the scatter is below 0.03 which is negligible compared to the values of $\bar{\eta}^{\mathrm{piso}}$ and $\bar{N}_{\mathrm{p}}^{\mathrm{piso}}$.

The fitted effective particle number $\bar{N}_{\mathrm{p}}^{\mathrm{piso}}$ is almost identical to the effective particle number $\bar{N}_{\mathrm{p}}^{\mathrm{mf}}$ of the mean-field model. Only for the highest fiber volume fractions $\bar{c}_{\mathrm{f}} = 15\% - 20\%$, there is a small difference. The scatter of $\bar{N}_{\mathrm{p}}^{\mathrm{piso}}$ is smaller than the yellow disk shaped markers, this is the reason why the scatter cannot be seen.

The error $e_{\mathrm{piso}}^{\mathrm{fit}} < 3.5\%$ is much smaller than the error $e_{\mathrm{piso}}^{\mathrm{mf}} < 13\%$, because of the difference in $\bar{\eta}$. The scatter of $e_{\mathrm{piso}}^{\mathrm{fit}}$ is acceptably small to consider the investigated volume element ($2.2l \times 2.2l \times 10d$) henceforth as RVE.

5.3.4 Isotropic case

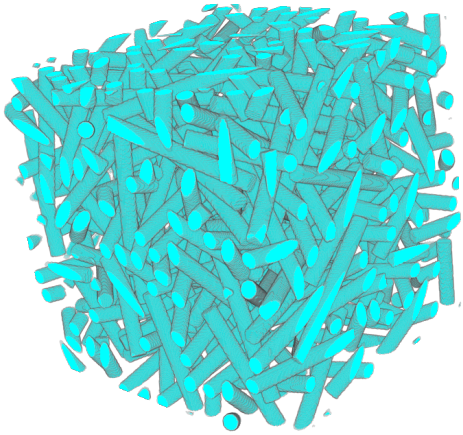

Figure 5.18: RVE of an *isotropic* (iso) microstructure made up by straight fibers.

Based on the estimations and the assumptions on the RVE (see sections 5.1.6 and 5.2.1), the size of the representative volume element for the isotropic case is considered to be: $L \times L \times L = 2.2l \times 2.2l \times 2.2l$, see for example Figure 5.18.

In the diagrams of Figure 5.19, the resulting fitted viscosity parameters $\bar{\eta}, \bar{N}_\mathrm{s}, \bar{N}_\mathrm{p}$, and the relative error of the fitted (e^fit) and of the mean-field (e^mf) model are shown in the case of isotropic microstructures, for fiber volume fractions in the range of 5%-20%.

The fitted effective viscosity $\bar{\eta}^\mathrm{iso}$ is consistently higher than the effective viscosity $\bar{\eta}^\mathrm{mf}$ of the mean-field model. The scatter of $\bar{\eta}^\mathrm{iso}$ is smaller than the cyan disk shaped markers, this is the reason why the scatter cannot be seen.

The fitted effective shear number $\bar{N}_\mathrm{s}^\mathrm{iso}$ is slightly lower than the effective shear number $\bar{N}_\mathrm{s}^\mathrm{mf}$ of the mean-field model, except for the highest fiber

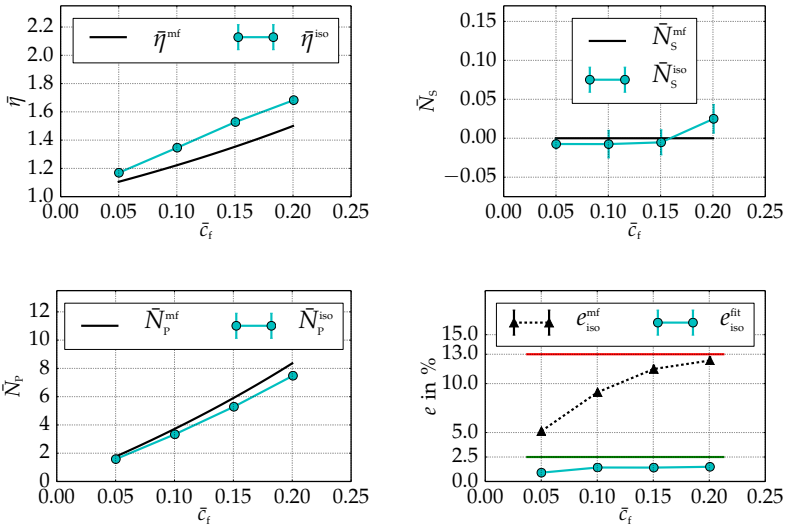

Figure 5.19: Mean-field (black) vs. fitted (cyan) viscosity parameters $\bar{\eta}$, $\bar{N}_{\mathrm{s}}$, $\bar{N}_{\mathrm{p}}$ and the error e considering the *isotropic* (iso) fiber-orientation state. The red and the green lines mark the upper limits of e.

volume fraction $\bar{c}_{\mathrm{f}} = 20\%$, where the relation is reverse. In spite of these observations, $\bar{N}_{\mathrm{s}}^{\mathrm{iso}}$ is very close to zero for all $\bar{c}_{\mathrm{f}}$. The maximum of the scatter is below 0.025, which is negligable compared to the values of $\bar{\eta}^{\mathrm{iso}}$ and $\bar{N}_{\mathrm{p}}^{\mathrm{iso}}$.

The fitted effective particle number $\bar{N}_{\mathrm{p}}^{\mathrm{iso}}$ slightly underestimates the effective particle number $\bar{N}_{\mathrm{p}}^{\mathrm{mf}}$ of the mean-field model. The scatter of $\bar{N}_{\mathrm{p}}^{\mathrm{iso}}$ is smaller than the cyan disk shaped markers, this is the reason why the scatter cannot be seen.

The error $e_{\mathrm{iso}}^{\mathrm{fit}} < 2.5\%$ is much smaller than the error $e_{\mathrm{iso}}^{\mathrm{mf}} < 13\%$, because of the difference in $\bar{\eta}$. The scatter of $e_{\mathrm{iso}}^{\mathrm{fit}}$ is smaller than the cyan disk shaped markers, this is the reason why the scatter cannot be seen. Thus the investigated volume element ($2.2l \times 2.2l \times 2.2l$) may henceforth be considered as RVE.

5.3.5 Frequently occurring case

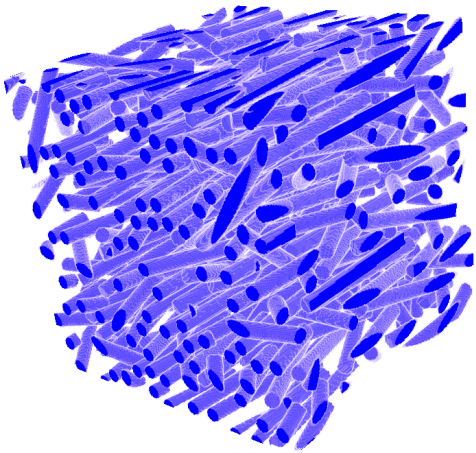

Figure 5.20: RVE of a *frequently occurring* (7715) microstructure made up by straight fibers.

Based on the estimations and the assumptions on the RVE (see sections 5.1.6 and 5.2.1), the size of the representative volume element for the frequently occurring case (Köbler et al., 2018) is considered to be: $L \times L \times L = 2.2l \times 2.2l \times 2.2l$, see for example Figure 5.20.

In the diagrams of Figure 5.21, the resulting fitted viscosity parameters $\bar{\eta}, \bar{N}_{\mathrm{s}}, \bar{N}_{\mathrm{p}}$, and the relative error of the fitted (e^{fit}) and of the mean-field (e^{mf}) model are shown in the case of the investigated frequently occurring microstructures, for fiber volume fractions in the range of 5%-20%.

The fitted effective viscosity $\bar{\eta}^{7715}$ is consistently higher than the effective viscosity $\bar{\eta}^{\mathrm{mf}}$ of the mean-field model. The scatter of $\bar{\eta}^{7715}$ is smaller than the blue disk shaped markers, this is the reason why the scatter cannot be seen.

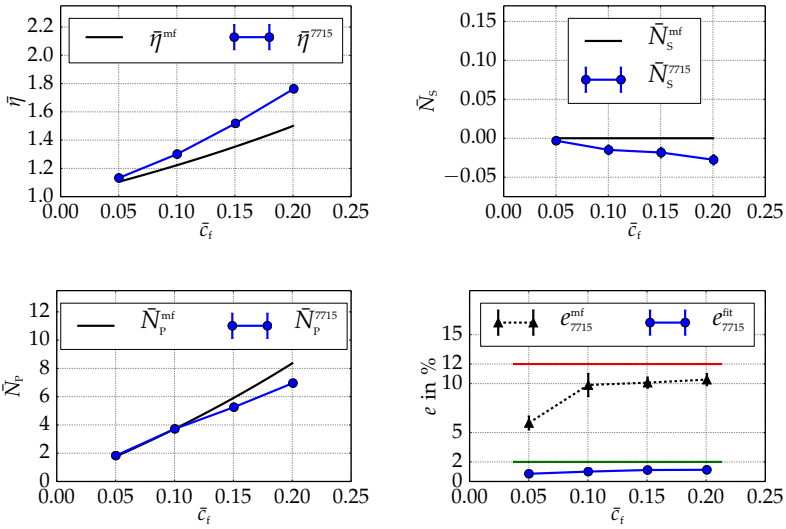

Figure 5.21: Mean-field (black) vs. fitted (blue) viscosity parameters $\bar{\eta}, \bar{N}_{\mathrm{s}}, \bar{N}_{\mathrm{p}}$ and the error e considering the *frequently occurring* (7715) fiber-orientation state. The red and the green lines mark the upper limits of e.

The fitted effective shear number $\bar{N}_{\mathrm{s}}^{7715}$ is slightly lower than the effective shear number $\bar{N}_{\mathrm{s}}^{\mathrm{mf}}$ of the mean-field model, but $\bar{N}_{\mathrm{s}}^{\mathrm{ud}}$ is very close to zero. The maximum of the scatter is below 0.01 which is negligible compared to the values of $\bar{\eta}^{7715}$ and $\bar{N}_{\mathrm{p}}^{7715}$.

The fitted effective particle number $\bar{N}_{\mathrm{p}}^{7715}$ slightly underestimates the effective particle number $\bar{N}_{\mathrm{p}}^{\mathrm{mf}}$ of the mean-field model. The scatter of $\bar{N}_{\mathrm{p}}^{7715}$ is smaller than the blue disk shaped markers, this is the reason why the scatter cannot be seen.

The error $e_{7715}^{\mathrm{fit}} < 2\%$ is much smaller than the error $e_{7715}^{\mathrm{mf}} < 12\%$, because of the difference in $\bar{\eta}$. The scatter of e_{7715}^{fit} is smaller than the blue disk shaped markers, this is the reason why the scatter cannot be seen. Thus the investigated volume element ($2.2l \times 2.2l \times 2.2l$) may henceforth be considered as RVE.

Chapter 6

Discussion

6.1 Fast approximation vs. determination of the effective viscosity tensor

Comparing the viscosity parameters of the fast approximation (see section 5.1.3) and the ones determined by $\bar{\mathbb{V}}^{\text{num}}$ (see section 5.3), it is observed that the resulting values are slightly different. Compare, for example, the grey curves of $\bar{\eta}$ in Figure 5.12 and the ones in Figure 5.13. The fast approximation slightly underestimates and the parameters of $\bar{\mathbb{V}}^{\text{num}}$ slightly overestimate the mean-field predictions of $\bar{\eta}$. Determining the viscosity parameters through $\bar{\mathbb{V}}^{\text{num}}$ is the more precise method. The fast approximation has the advantage that only three load cases have to be computed to get the approximation of the viscosity parameters, instead of computing five load cases and conducting the fitting procedure for each of the investigated numerous microstructures, as described in section 5.1. The approximated viscosity parameters substituted into (2.12) result exactly the same stress response as the numerical model only for the three special load cases (5.3)-(5.5), but they do not give exactly the same values for other load cases. Furthermore, the error measures e^{fit} (5.15) and e^{mf} (5.16) can be well defined only in the case of determining $\bar{\mathbb{V}}^{\text{num}}$. Therefore, all viscosity parameters in and after subsection 5.3 are determined through the more precise method – through the determination of $\bar{\mathbb{V}}^{\text{num}}$ –, as described in subsection 5.2.

6.2 Single fiber vs. unidirectional fibers

The resulting viscosity parameters and the errors – obtained by the parameter fitting method – of a single fiber in a periodic cell (see section 5.3.1) and those of the unidirectional fibers (see section 5.3.2) are compared in the diagrams of the Figures 6.1-6.4.

The resulting effective viscosities have the ordering: $\bar{\eta}^{\mathrm{mf}} \leq \bar{\eta}^{\mathrm{sf}} \leq \bar{\eta}^{\mathrm{ud}}$, see Figure 6.1. The largest relative difference between $\bar{\eta}^{\mathrm{ud}}$ and $\bar{\eta}^{\mathrm{sf}}$ is about 6% at the highest investigated fiber volume fraction $\bar{c}_{\mathrm{f}} = 0.2$.

The relations considering the effective shear number for $\bar{c}_{\mathrm{f}} \geq 0.1$ are reversed, namely $\bar{N}_{\mathrm{s}}^{\mathrm{mf}} \geq \bar{N}_{\mathrm{s}}^{\mathrm{sf}} \geq \bar{N}_{\mathrm{s}}^{\mathrm{ud}}$, see Figure 6.2. Note that the fitted values of $\bar{N}_{\mathrm{s}}^{\mathrm{sf}}$ and $\bar{N}_{\mathrm{s}}^{\mathrm{ud}}$ are mainly negative, but they are very close to the mean-field predicted zero value, relative to the magnitudes of $\bar{\eta}$ and $\bar{N}_{\mathrm{p}}$.

A difference of factor two to three is observed in the case of the effective particle number comparing $\bar{N}_{\mathrm{p}}^{\mathrm{sf}}$ to $\bar{N}_{\mathrm{p}}^{\mathrm{ud}}$, whereas $\bar{N}_{\mathrm{p}}^{\mathrm{mf}}$ and $\bar{N}_{\mathrm{p}}^{\mathrm{ud}}$ are almost identical for the investigated fiber volume fraction range, see Figure 6.3.

The negligible scatter of $\bar{\eta}^{\mathrm{ud}}, \bar{N}_{\mathrm{s}}^{\mathrm{ud}}$ and $\bar{N}_{\mathrm{p}}^{\mathrm{ud}}$ and the large difference between $\bar{N}_{\mathrm{p}}^{\mathrm{ud}}$ to $\bar{N}_{\mathrm{p}}^{\mathrm{sf}}$ show that the considered $2.2l \times 10d \times 10d$ sized volume element is an RVE, but a single fiber in a periodic cell is not an RVE, for *randomly* distributed unidirectionally aligned fibers.

Considering the errors of the different methods relative to the numerical reference solution $\bar{\mathbb{V}}_{\mathrm{ud}}^{\mathrm{num}}$, the relations $e_{\mathrm{ud}}^{\mathrm{fit}} \leq e_{\mathrm{ud}}^{\mathrm{mf}} \leq e_{\mathrm{ud}}^{\mathrm{sf}}$ are observed, see Figure 6.4. Note that the vertical axis has a logarithmic scale. The three considered errors have different orders of magnitude: $e_{\mathrm{ud}}^{\mathrm{fit}} \sim 1\%, e_{\mathrm{ud}}^{\mathrm{mf}} \sim 10\%$ and $e_{\mathrm{ud}}^{\mathrm{sf}} \sim 100\%$. Taking the scatters in account, the upper limits of the errors are: $e_{\mathrm{ud}}^{\mathrm{fit}} \leq 2.5\%,\ e_{\mathrm{ud}}^{\mathrm{mf}} \leq 18\%$ and $e_{\mathrm{ud}}^{\mathrm{sf}} \leq 200\%$.

The main conclusion of this section is that the costly microstructure generation, the computations on them, the fitting procedure and the RVE-determination are worth to carry out, because the error of the fitted model – relative to $\bar{\mathbb{V}}_{\mathrm{ud}}^{\mathrm{num}}$ – is tenth and hundredth smaller than the errors of the mean-field and the single fiber model, respectively.

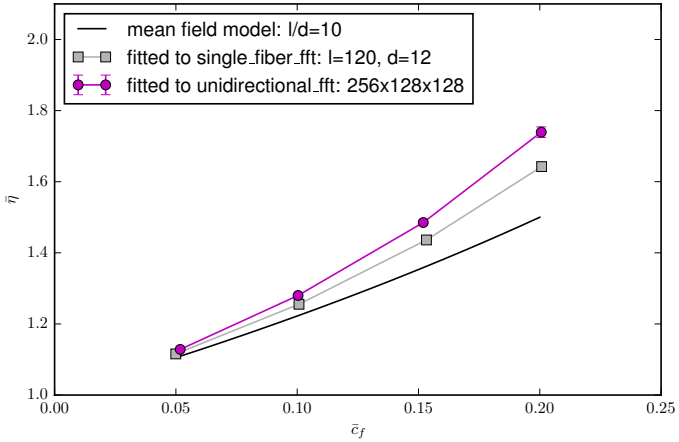

Figure 6.1: Comparison of the *effective viscosity* $\bar{\eta}$ of the single fiber (sf) and that of the unidirectional (ud) model. The black curve depicts the prediction of the mean-field (mf) model.

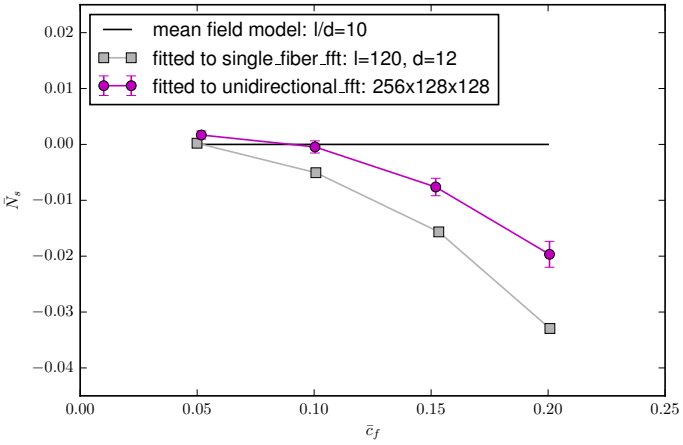

Figure 6.2: Comparison of the *shear number* $\bar{N}_s$ of the single fiber (sf) and that of the unidirectional (ud) model. The black curve depicts the prediction of the mean-field (mf) model.

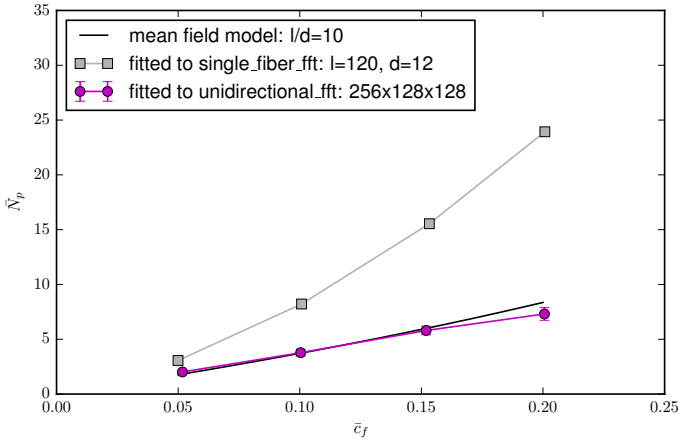

Figure 6.3: Comparison of the *particle number* $\bar{N}_\mathrm{p}$ of the single fiber (sf) and that of the unidirectional (ud) model. The black curve depicts the prediction of the mean-field (mf) model.

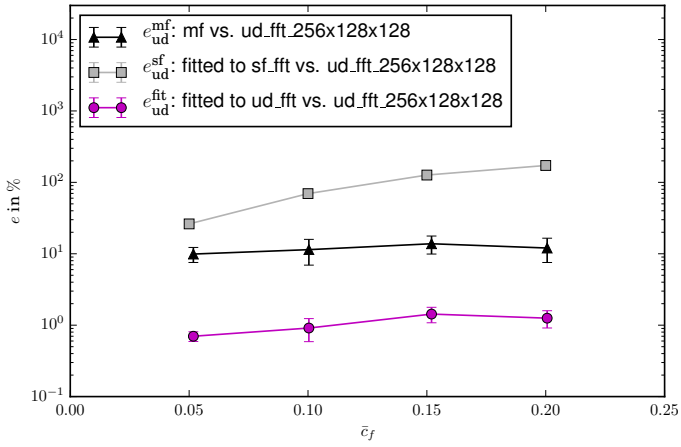

Figure 6.4: Comparison of the *error* e_ud of the single fiber (sf) and that of the unidirectional (ud) model. The black curve depicts the prediction of the mean-field (mf) model.

6.3 On orientation averaging

In this section, the results of the investigated four orientation cases (ud, iso, piso, 7715) are compared. The goal of the comparison is to evaluate which of the following three approaches is the most appropriate for engineering applications to model the orientation dependence of the effective viscosity tensor. The three considered approaches are:

$$\bar{\mathbb{V}}^{\text{model-1}} = \bar{\mathbb{V}}(\bar{\eta}, \bar{N}_{\text{s}}, \bar{N}_{\text{p}}, \bar{\mathbb{N}}), \tag{6.1}$$

$$\bar{\mathbb{V}}^{\text{model-2}} = \bar{\mathbb{V}}(\bar{\eta}(\bar{\mathbb{N}}), \bar{N}_{\text{s}}(\bar{\mathbb{N}}), \bar{N}_{\text{p}}(\bar{\mathbb{N}}), \bar{\mathbb{N}}), \tag{6.2}$$

$$\bar{\mathbb{V}}^{\text{model-3}} = \bar{\mathbb{V}}^{\text{fft}}(\eta_{\text{m}}, r_{\text{a}}, \bar{c}_f, \boldsymbol{n}_\alpha(\boldsymbol{x})). \tag{6.3}$$

Model-1 is the simplest approach, assuming that the viscosity parameters are orientation independent and that orientation averaging – see equations (2.11) and (2.12) – is justified. Model-2 assumes that the viscosity parameters are unique for each orientation case and they have to be identified for each orientation state separately. Model-3 is the most complex one which assumes that there are no unique viscosity parameters, e.g., because of large scatter of the results, which would mean that an RVE does not exist and that the viscosity tensor has to be determined for each spatial distribution ($\boldsymbol{n}_\alpha(\boldsymbol{x})$) of the fibers separately. As already shown in section 5.3, there exists an RVE for each investigated orientation state, although their sizes are different. This implies that the most complex approach (model-3) can be simplified, and the correctness of the simpler approach (model-2) can be supposed.

In the diagrams of the Figures 6.5-6.8, the viscosity parameters and the errors of the four investigated cases are compared. The curves of the considered four orientation cases are almost identical, except for $\bar{N}_{\text{s}}$ which value is, however, almost zero. This implies that the viscosity parameters are orientation state independent and that model-2 can be further simplified, i.e., model-1 with orientation averaging is justified for $r_{\text{a}} = 10$.

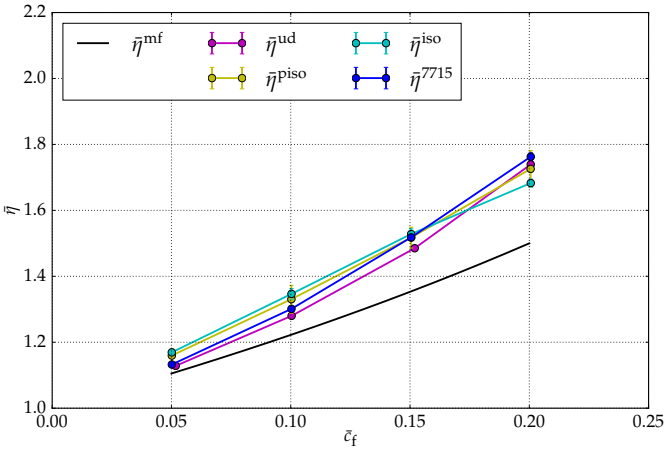

Figure 6.5: Comparison of the *effective viscosity* $\bar{\eta}$ of the different orientation states. The black curve depicts the prediction of the mean-field (mf) model.

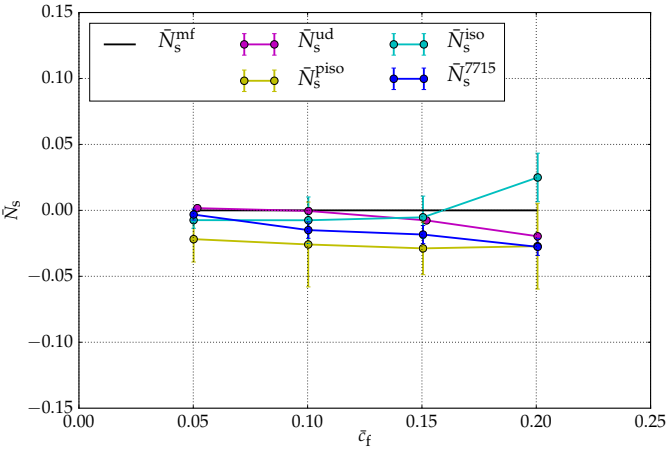

Figure 6.6: Comparison of the *shear number* $\bar{N}_{\mathrm{s}}$ of the different orientation states. The black curve depicts the prediction of the mean-field (mf) model.

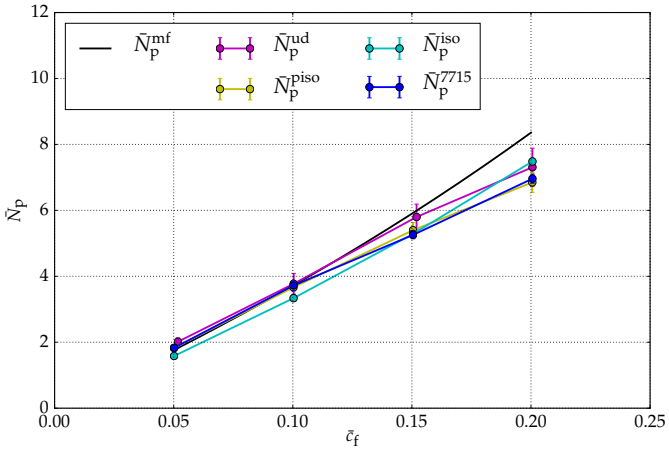

Figure 6.7: Comparison of the *particle number* $\bar{N}_\mathrm{p}$ of the different orientation states. The black curve depicts the prediction of the mean-field (mf) model.

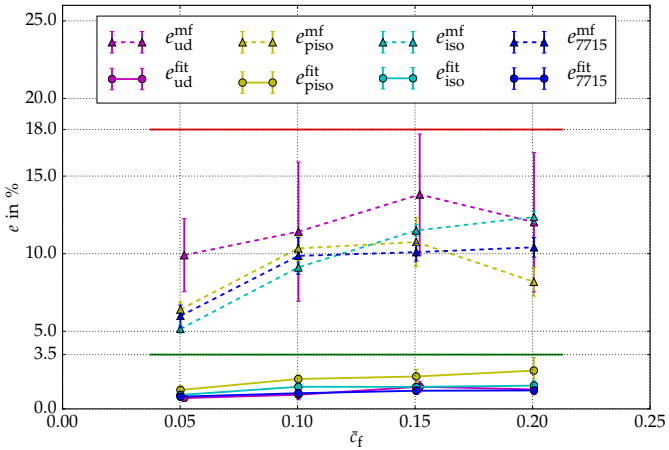

Figure 6.8: Comparison of the *error* e of the different orientation states. The dashed curves depict the error of the mean-field (mf) model.

6.4 RVE size of short-fiber microstructures

Based on all the aforementioned results, it can be stated that a cubic volume element of the size $2.2l \times 2.2l \times 2.2l$ is an RVE for every fiber-orientation state, where l denotes the constant length of the straight and rigid fibers. For special orientation cases, e.g., for unidirectional or planar isotropic ones, the RVE size is even smaller. These observation were obtained by considering short fibers with constant aspect ratio $r_\mathrm{a} = 10$. However, for fiber systems with higher or mixed aspect ratios, it should be always tested if the above statement is true, e.g., through repeating the analysis of section 5.2, and investigating the scatter in the results.

6.5 Recommendations for form-filling simulations

The main difference between the mean-field and the fitted models (see Figure 6.8) is caused by the differences in $\bar{\eta}$ and $\bar{N}_\mathrm{p}$ (see Figures 6.5-6.7). Note that the magnitudes of $\bar{N}_\mathrm{s}$ are mainly negative but they are very close to the mean-field predicted zero value, relative to the magnitudes of $\bar{\eta}$ and $\bar{N}_\mathrm{p}$. With the following analytical approximations

$$\bar{\eta}^\mathrm{ap} := \eta_\mathrm{m}\left(1 + \frac{2\bar{c}_\mathrm{f}}{1-\sqrt{\bar{c}_\mathrm{f}}}\right), \tag{6.4}$$

$$\bar{N}_\mathrm{s}^\mathrm{ap} := \bar{N}_\mathrm{s}^\mathrm{mf} = 0, \tag{6.5}$$

$$\bar{N}_\mathrm{p}^\mathrm{ap} := 35.6\ \bar{c}_\mathrm{f}, \tag{6.6}$$

the appropriate orange curves depicted in Figure 6.9 are obtained. Using the viscosity parameters $\bar{\eta}^\mathrm{ap}, \bar{N}_\mathrm{s}^\mathrm{mf}$ and $\bar{N}_\mathrm{p}^\mathrm{ap}$ within equation (2.12), we get an *analytical* approximation of the numerical viscosity tensor $\bar{\mathbb{V}}^\mathrm{num}$ for $r_\mathrm{a} = 10$. The overall error of the fitted and the approximated mod-

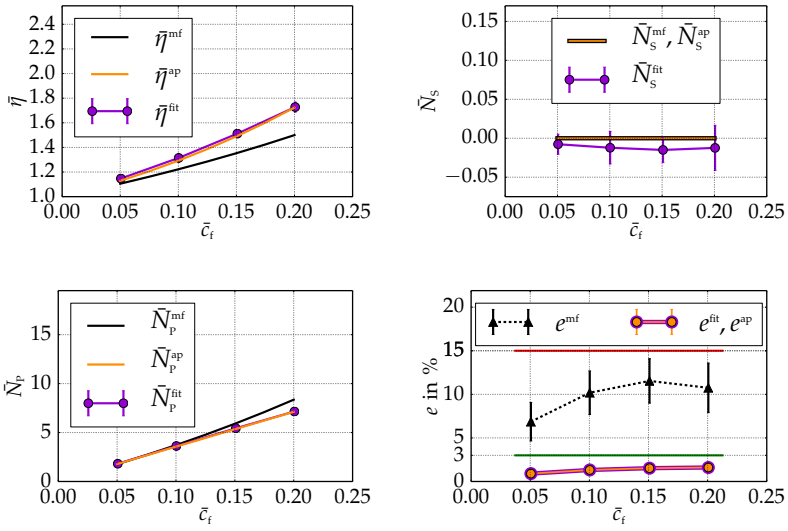

Figure 6.9: Mean-field (black) vs. fitted (purple) vs. approximated (orange) viscosity parameters $\bar{\eta}$, $\bar{N}_s$, $\bar{N}_p$ and the error e considering *all* investigated fiber-orientation states. The red and the green horizontal lines mark the upper limits of e.

els $e^{fit} = e^{ap} < 3\%$ is one order of magnitude smaller than the overall error of the mean-field model $e^{mf} < 15\%$, see Figure 6.9.

The analytical approximation $\bar{\mathbb{V}}^{ap} = \bar{\mathbb{V}}(\bar{\eta}^{ap}, \bar{N}_s^{mf}, \bar{N}_p^{ap}, \bar{\mathbb{N}})$ with the equations (2.12) and (6.4)-(6.6) is recommended to be used for form-filling simulations.

Chapter 7

Summary, conclusions and outlook

7.1 Summary and conclusions

The present work deals with the flow-induced anisotropy of fiber suspensions and compares different modeling approaches to describe this phenomenon for form-filling simulations.

Using orientation tensors of the first kind, the general form of the effective viscosity tensor is derived in Chapter 2. The conclusion of the derivation is that in the case of straight rigid fibers and an incompressible fluid, three parameters – the effective scalar viscosity, the shear number and the particle number – are sufficient to describe the dependence of the viscosity tensor on the constitutive behavior of matrix and fibers.

In Chapter 3 it is shown that it is much more efficient to model the fiber orientation of straight rigid fibers immersed in an incompressible fluid flow by applying orientation tensors instead of modeling the fibers individually in terms of their normalized orientation vectors. This observation is made based on Jeffery's equation and the invariant-based optimal fitting closure which is slower but more suitable than the quadratic closure approximation.

The microstructure dependence of the three viscosity parameters is derived by applying Mori-Tanaka's mean-field homogenization method

based on Eshelby's tensor, see Chapter 4. The considered microstructure properties are the fiber volume fraction, the aspect ratio and the fluid viscosity. The resulting complex equations are mathematically simplified into convenient formulas without a notable change in precision.

The investigated, synthetically generated microstructure types – on which the numerical computations are carried out – are presented in Chapter 5. Based on preliminary full-field simulations, the size of the RVE for each examined orientation case is estimated. One of the most important parts of this work is the numerical computation of the effective viscosity tensors, based on five load cases per considered microstructure. The viscosity parameters corresponding to the numerical effective viscosity tensors are determined by minimizing the relative error of the Frobenius norm in a least-squares manner. The resulting effective scalar viscosity, the shear number and the particle number of the mean-field and the full-field homogenization methods are compared to each other, and their errors, relative to the numerically computed effective viscosity tensors, are given for all five investigated orientation cases.

It is shown in Chapter 6 that a single fiber in a periodic cell is not an RVE for the unidirectional fiber-orientation state, and it is concluded that a cubic volume element with edge sizes 2.2 times larger than the length of the considered straight rigid fibers is a representative volume element. Furthermore, it is observed that the relative errors of the full-field model are about one order of magnitude smaller than the errors of the mean-field model. The final conclusion is that the compact analytical approximations of the viscosity parameters, derived based on the numerical results of the presented full-field computations, lead to the same precision regarding the effective viscosity tensor as the numerically identified viscosity parameters. The compact approximations of the viscosity parameters are recommended to be used in form-filling

simulations for modeling the flow-induced anisotropic effective viscosity of fiber suspensions in an efficient way.

7.2 Outlook

The numerical results in this work were computed with the use of only 8 GB RAM. With the use of more memory, representative volume elements of higher fiber volume fractions and fiber systems with larger/mixed aspect ratios could be investigated. That would be interesting, e.g., for engineering applications in the field of injection- and compression molding.

In the present work, the nonlinearity of the fluid viscosity is neglected. To account for this effect, the simplest way is to substitute the deformation rate dependent viscosity of the fluid into the equations of the viscosity parameters. It would be worth to investigate whether the obtained formulas match the results of shear rate dependent full-field simulations, and whether the results of form-filling simulations with such a nonlinear material model are close to the results of form-filling measurements.

The temperature dependence of the viscosity could be similarly modeled and numerically validated as the nonlinearity mentioned above.

A challenging task for further research work is the development of effective-viscosity models considering flexible fibers in the suspension.

For form-filling simulations another interesting question is how the evolution and the anisotropy of the flow front, as well as the spatial and temporal change of the fiber volume fraction could be modeled.

For fiber volume fractions $\bar{c}_\mathrm{f} > 0.5$ and for matrix materials which cannot be considered as fluid, other modeling techniques have to be developed.

Appendix A

Investigated microstructures

Some of the investigated synthetic microsturtures are depicted on the following pages.

A.1 Unidirectional synthetic microstructures

Figure A.1.1: Eight series of the investigated unidirectional synthetic microstructures. The fiber volume fractions from left to right are: 5%, 10%, 15% and 20%.

A.2 Planar isotropic synthetic microstructures

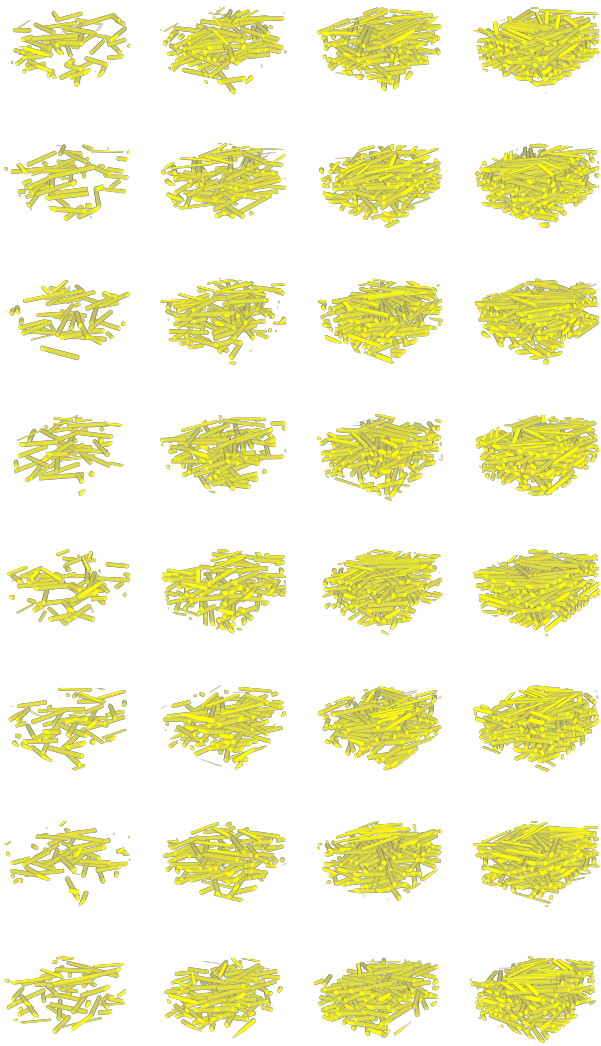

Figure A.2.1: Eight series of the investigated planar isotropic synthetic microstructures. The fiber volume fractions from left to right are: 5%, 10%, 15% and 20%.

A.3 Isotropic synthetic microstructures

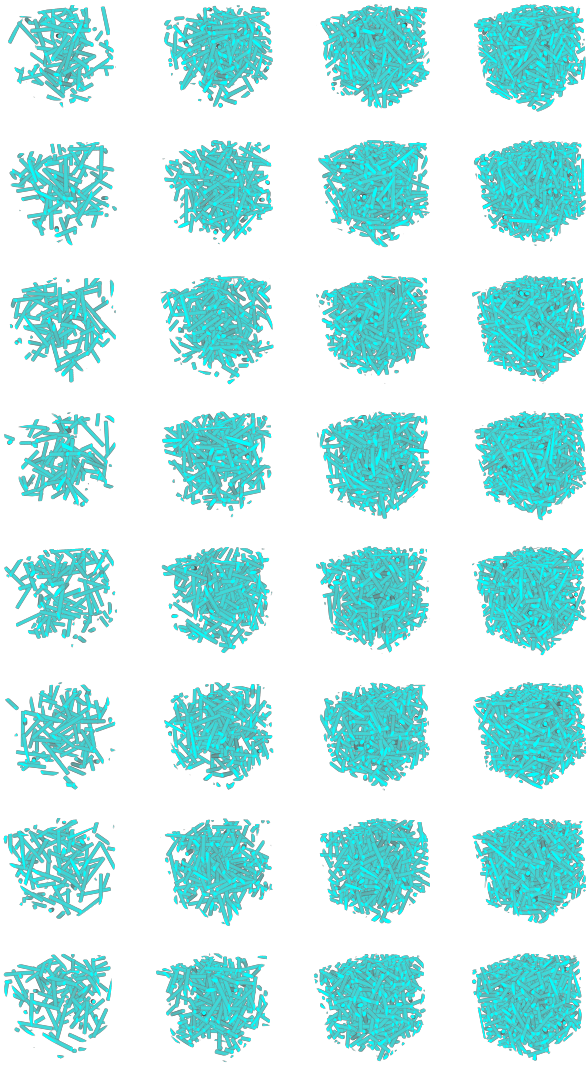

Figure A.3.1: Eight series of the investigated isotropic synthetic microstructures. The fiber volume fractions from left to right are: 5%, 10%, 15% and 20%.

A.4 Frequently occurring synth. microstructures

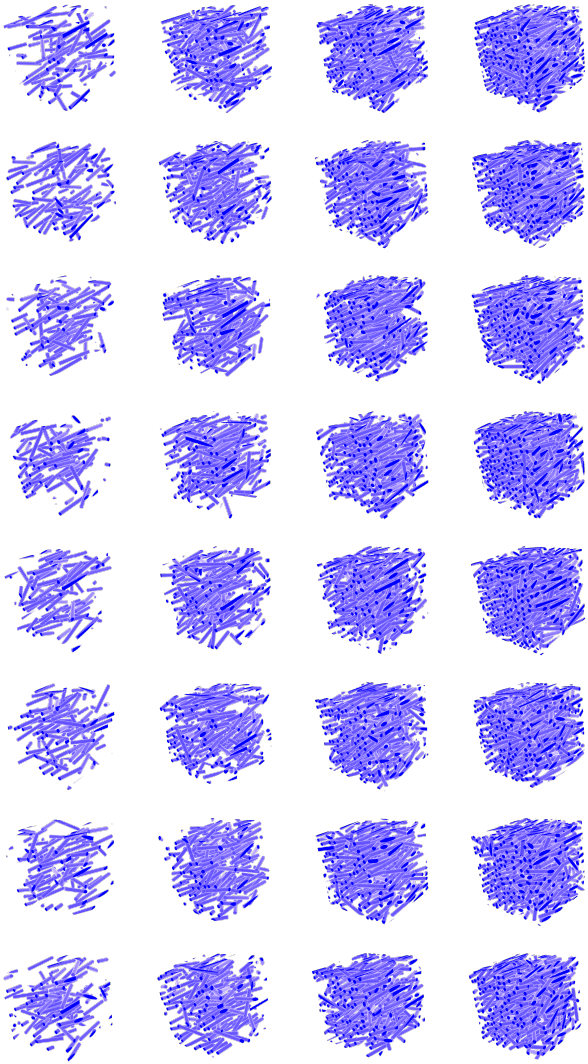

Figure A.4.1: Eight series of the investigated frequently occurring synthetic microstructures. The fiber volume fractions from left to right are: 5%, 10%, 15% and 20%.

Bibliography

Advani, S. G., Tucker III, C. L., 1987. The use of tensors to describe and predict fiber orientation in short fiber composites. Journal of Rheology 31 (8), 751–784.

Advani, S. G., Tucker III, C. L., 1990. Closure approximations for three-dimensional structure tensors. Journal of Rheology 34 (3), 367–386.

Alexandrou, A., Mitsoulis, E., 2007. Transient planar squeeze flow of semi-concentrated fiber suspensions using the Dinh–Armstrong model. Journal of Non-Newtonian Fluid Mechanics 146 (1-3), 114–124.

Barzilai, J., Borwein, J. M., 1988. Two-point step size gradient methods. IMa Journal of Numerical Analysis 8 (1), 141–148.

Bay, R. S., Tucker III, C. L., 1992a. Fiber orientation in simple injection moldings. Part I: Theory and numerical methods. Polymer Composites 13 (4), 317–331.

Bay, R. S., Tucker III, C. L., 1992b. Fiber orientation in simple injection moldings. Part II: Experimental results. Polymer Composites 13 (4), 332–341.

Bertóti, R., Böhlke, T., 2016. Flow-induced anisotropic viscosity in short fiber reinforced polymers. PAMM 16 (1), 589–590.

Bertóti, R., Böhlke, T., 2017a. Fiber-Orientation-Evolution Models for Compression Molding of Fiber Reinforced Polymers. Proceedings of the 7th GACM Colloquium on Computational Mechanics, Stuttgart, 611–614.

Bertóti, R., Böhlke, T., 2017b. Flow-induced anisotropic viscosity in short FRPs. Mechanics of Advanced Materials and Modern Processes 3 (1), 1–12.

Bertóti, R., Wicht, D., Schneider, M., Böhlke, T., 2020a. Anisotropic effective viscosity of short-fiber suspensions. ICTAM 2020+1, accepted short paper, 1–2.

Bertóti, R., Wicht, D., Schneider, M., Hrymak, A., Böhlke, T., 2020b. A computational investigation of the effective viscosity of short-fiber reinforced thermoplastics by an FFT-based method. submitted paper, 1–30.

Boehler, J.-P., 1987. Applications of tensor functions in solid mechanics. Vol. 292 of CISM International Centre for Mechanical Sciences. Springer, New York.

Böhlke, T., 2006. Texture simulation based on tensorial Fourier coefficients. Computers & Structures 84 (17-18), 1086–1094.

Böhlke, T., Bertram, A., 2001. The evolution of Hooke's law due to texture development in FCC polycrystals. International Journal of Solids and Structures 38 (52), 9437–9459.

Böhlke, T., Bertram, A., Krempl, E., 2003. Modeling of deformation induced anisotropy in free-end torsion. International Journal of Plasticity 19 (11), 1867–1884.

Brenner, H., 1974. Rheology of a dilute suspension of axisymmetric Brownian particles. International Journal of Multiphase Flow 1 (2), 195–341.

Buck, F., Brylka, B., Müller, V., Müller, T., Weidenmann, K. A., Hrymak, A. N., Henning, F., Böhlke, T., 2015. Two-scale structural mechanical modeling of long fiber reinforced thermoplastics. Composites Science and Technology 117, 159–167.

Castaneda, P. P., Suquet, P., 1997. Nonlinear composites. In: Advances in Applied Mechanics. Vol. 34. Elsevier, pp. 171–302.

Chung, D. H., Kwon, T. H., 2002a. Fiber orientation in the processing of polymer composites. Korea-Australia Rheology Journal 14 (4), 175–188.

Chung, D. H., Kwon, T. H., 2002b. Numerical studies of fiber suspensions in an axisymmetric radial diverging flow: the effects of modeling and numerical assumptions. Journal of Non-Newtonian Fluid Mechanics 107 (1-3), 67–96.

Cintra Jr, J. S., Tucker III, C. L., 1995. Orthotropic closure approximations for flow-induced fiber orientation. Journal of Rheology 39 (6), 1095–1122.

Cross, M. M., 1970. Kinetic interpretation of non-Newtonian flow. Journal of Colloid and Interface Science 33 (1), 30–35.

Dinh, S. M., Armstrong, R. C., 1984. A rheological equation of state for semiconcentrated fiber suspensions. Journal of Rheology 28 (3), 207–227.

Doi, M., 1981. Molecular dynamics and rheological properties of concentrated solutions of rodlike polymers in isotropic and liquid crystalline phases. Journal of Polymer Science: Polymer Physics Edition 19, 243.

Ericksen, J., 1959. Anisotropic fluids. Archive for Rational Mechanics and Analysis 4 (1), 231–237.

Ericksen, J., 1960a. Theory of anisotropic fluids. Transactions of the Society of Rheology 4 (1), 29–39.

Ericksen, J., 1960b. Transversely isotropic fluids. Kolloid-Zeitschrift 173 (2), 117.

Eschbach, A. R., Dec. 21 1993. Dynamic shear rheometer and method. US Patent 5,271,266.

Eshelby, J. D., 1957. The determination of the elastic field of an ellipsoidal inclusion, and related problems. Proceedings of the Royal Society of London. Series A. Mathematical and Physical Sciences 241 (1226), 376–396.

Ferry, J. D., 1980. Viscoelastic properties of polymers. John Wiley & Sons, New York.

Fiolka, M., 2008. Theorie und Numerik volumetrischer Schalenelemente zur Delaminationsanalyse von Faserverbundlaminaten. Kassel University Press GmbH, Kassel.

Folgar, F., Tucker III, C., 1984. Orientation behavior of fibers in concentrated suspensions. Journal of Reinforced Plastics and Composites 3 (2), 98–119.

Fu, S.-Y., Lauke, B., Mäder, E., Yue, C.-Y., Hu, X., 2000. Tensile properties of short-glass-fiber-and short-carbon-fiber-reinforced polypropylene composites. Composites Part A: Applied Science and Manufacturing 31 (10), 1117–1125.

Gitman, I., Askes, H., Sluys, L., 2007. Representative volume: existence and size determination. Engineering Fracture Mechanics 74 (16), 2518–2534.

Gross, D., Seelig, T., 2017. Fracture mechanics: with an introduction to micromechanics. Springer, Berlin.

Halmos, P. R., 1958. Finite-dimensional vector spaces, 2nd Edition. Van Nostrand, New York.

Hand, G. L., 1962. A theory of anisotropic fluids. Journal of Fluid Mechanics 13 (1), 33–46.

Hashin, Z., Shtrikman, S., 1962. A variational approach to the theory of the elastic behaviour of polycrystals. Journal of the Mechanics and Physics of Solids 10 (4), 343–352.

Heinen, K., 2007. Mikrostrukturelle Orientierungszustände strömender Polymerlösungen und Fasersuspensionen. Doctoral thesis, Universität Dortmund.

Hinch, E., Leal, L., 1972. The effect of Brownian motion on the rheological properties of a suspension of non-spherical particles. Journal of Fluid Mechanics 52 (4), 683–712.

Holzapfel, G., 2000. Nonlinear solid mechanics. A Continuum Approach for Engineering. John Wiley & Sons, Chichester.

Jeffery, G. B., 1922. The motion of ellipsoidal particles immersed in a viscous fluid. Proceedings of the Royal Society of London. Series A, Containing Papers of a Mathematical and Physical Character 102 (715), 161–179.

Junk, M., Illner, R., 2007. A new derivation of Jeffery's equation. Journal of Mathematical Fluid Mechanics 9 (4), 455–488.

Kammoun, S., Doghri, I., Adam, L., Robert, G., Delannay, L., 2011. First pseudo-grain failure model for inelastic composites with misaligned short fibers. Composites Part A: Applied Science and Manufacturing 42 (12), 1892–1902.

Kanatani, K.-I., 1984. Distribution of directional data and fabric tensors. International Journal of Engineering Science 22 (2), 149–164.

Köbler, J., Schneider, M., Ospald, F., Andrä, H., Müller, R., 2018. Fiber orientation interpolation for the multiscale analysis of short fiber reinforced composite parts. Computational Mechanics 61 (6), 729–750.

Koszkul, J., Nabialek, J., 2004. Viscosity models in simulation of the filling stage of the injection molding process. Journal of Materials Processing Technology 157 (158), 183–187.

Latz, A., Strautins, U., Niedziela, D., 07 2010. Comparative numerical study of two concentrated fiber suspension models. Journal of Non-Newtonian Fluid Mechanics 165 (13-14), 764–781.

Lipscomb II, G., Denn, M. M., Hur, D., Boger, D. V., 1988. The flow of fiber suspensions in complex geometries. Journal of Non-Newtonian Fluid Mechanics 26 (3), 297–325.

Mandel, J., 1965. Généralisation de la théorie de plasticité de WT Koiter. International Journal of Solids and Structures 1 (3), 273–295.

Mardia, K. V., Jupp, P. E., 2009. Directional statistics. Vol. 494. John Wiley & Sons, Chichester.

Mezi, D., Ausias, G., Advani, S. G., Férec, J., 2019. Fiber suspension in 2D nonhomogeneous flow: The effects of flow/fiber coupling for Newtonian and power-law suspending fluids. Journal of Rheology 63 (3), 405–418.

Montgomery-Smith, S., He, W., Jack, D. A., Smith, D. E., 2011a. Exact tensor closures for the three-dimensional Jeffery's equation. Journal of Fluid Mechanics 680, 321–335.

Montgomery-Smith, S., Jack, D., Smith, D. E., 2011b. The fast exact closure for Jeffery's equation with diffusion. Journal of Non-Newtonian Fluid Mechanics 166 (7-8), 343–353.

Mori, T., Tanaka, K., 1973. Average stress in matrix and average elastic energy of materials with misfitting inclusions. Acta Metallurgica 21 (5), 571–574.

Newton, I., 1999. The Principia: mathematical principles of natural philosophy. University of California Press, Bekerley.

Oseen, C., 1933. The theory of liquid crystals. Transactions of the Faraday Society 29 (140), 883–899.

Ospald, F., 2014. Numerical simulation of injection molding using OpenFOAM. PAMM, Fürth 14 (1), 673–674.

Papenfuss, C., Muschik, W., 2018. Macroscopic Internal Variables and Mesoscopic Theory: A Comparison Considering Liquid Crystals. Entropy 20 (1), 81.

Phan-Thien, N., Fan, X.-J., Tanner, R., Zheng, R., 2002. Folgar–Tucker constant for a fibre suspension in a Newtonian fluid. Journal of Non-Newtonian Fluid Mechanics 103 (2-3), 251–260.

Phan-Thien, N., Graham, A. L., 1991. A new constitutive model for fiber suspensions: flow past a sphere. Rheol Acta 30, 44–57.

Phelps, J., Tucker III, C., 2009. An anisotropic rotary diffusion model for fiber orientation in short-and long-fiber thermoplastics. Journal of Non-Newtonian Fluid 156 (3), 165–176.

Pipes, R. B., Hearle, J., Beaussart, A., Sastry, A., Okine, R., 1991. A constitutive relation for the viscous flow of an oriented fiber assembly. Journal of Composite Materials 25 (9), 1204–1217.

Poslinski, A., Ryan, M., Gupta, R., Seshadri, S., Frechette, F., 1988. Rheological Behavior of Filled Polymeric Systems I. Yield Stress and Shear-Thinning Effects. Journal of Rheology 32 (7), 703–735.

Schneider, M., 2016. On the effective viscosity of a periodic suspension–analysis of primal and dual formulations for Newtonian and non-Newtonian solvents. Mathematical Methods in the Applied Sciences 39 (12), 3309–3327.

Schneider, M., 2017. The sequential addition and migration method to generate representative volume elements for the homogenization of short fiber reinforced plastics. Computational Mechanics 59 (2), 247–263.

Schneider, M., 2019. On the Barzilai-Borwein basic scheme in FFT-based computational homogenization. International Journal for Numerical Methods in Engineering 118 (8), 482–494.

Schneider, M., Ospald, F., Kabel, M., 2016. Computational homogenization of elasticity on a staggered grid. International Journal for Numerical Methods in Engineering 105 (9), 693–720.

Shaqfeh, E. S., Fredrickson, G. H., 1990. The hydrodynamic stress in a suspension of rods. Physics of Fluids A: Fluid Dynamics 2 (1), 7–24.

Sommer, D. E., Favaloro, A. J., Pipes, R. B., 2018. Coupling anisotropic viscosity and fiber orientation in applications to squeeze flow. Journal of Rheology 62 (3), 669–679.

Spencer, A. J. M., et al., 1984. Continuum theory of the mechanics of fibre-reinforced composites. Vol. 282. Springer, New York.

Tandon, G., Weng, G., 1984. The effect of aspect ratio of inclusions on the elastic properties of unidirectionally aligned composites. Polymer Composites 5 (4), 327–333.

Tang, L., Altan, M. C., 1995. Entry flow of fiber suspensions in a straight channel. Journal of Non-Newtonian Fluid Mechanics 56 (2), 183–216.

Torquato, S., 2002. Random Heterogeneous Materials: Microstructure and Macroscopic Properties. Vol. 16. Springer, New York, science+Business Media.

Tseng, H. C., Chang, R. Y., Hsu, C. H., Oct. 29 2013a. Method and computer readable media for determining orientation of fibers in a fluid. US Patent 8,571,828.

Tseng, H.-C., Chang, R.-Y., Hsu, C.-H., 2013b. Phenomenological improvements to predictive models of fiber orientation in concentrated suspensions. Journal of Rheology 57 (6), 1597–1631.

Tseng, H.-C., Chang, R.-Y., Hsu, C.-H., 2016. An objective tensor to predict anisotropic fiber orientation in concentrated suspensions. Journal of Rheology 60 (2), 215–224.

Tseng, H.-C., Favaloro, A. J., 2019. The use of informed isotropic constitutive equation to simulate anisotropic rheological behaviors in fiber suspensions. Journal of Rheology 63 (2), 263–274.

Tucker III, C. L., 1991. Flow regimes for fiber suspensions in narrow gaps. Journal of Non-Newtonian Fluid Mechanics 39 (3), 239–268.

Verleye, V., 1993. Prediction of fiber orientation in complex injection molded parts. ASME Appl. Mech. Division 175, 139–163.

Walpole, L., 1969. On the overall elastic moduli of composite materials. Journal of the Mechanics and Physics of Solids 17 (4), 235–251.

Wang, J., O'Gara, J., Tucker III, C., 2008. An objective model for slow orientation kinetics in concentrated fiber suspensions: Theory and rheological evidence. Journal of Rheology 52 (5), 1179–1200.

Weise, M., Meyer, A., 2010. Grundgleichungen für transversal isotropes Materialverhalten. Vol. 10-03. Chemnitz Scientific Computing Preprints, Chemnitz.

Wicht, D., Schneider, M., Böhlke, T., 2020. An efficient solution scheme for small-strain crystal-elasto-viscoplasticity in a dual framework. Computer Methods in Applied Mechanics and Engineering 358, 1–25.

Williams, M. L., Landel, R. F., Ferry, J. D., 1955. The temperature dependence of relaxation mechanisms in amorphous polymers and other glass-forming liquids. Journal of the American Chemical Society 77 (14), 3701–3707.

Willis, J. R., 1977. Bounds and self-consistent estimates for the overall properties of anisotropic composites. J. Mech. Phys. Solids 25, 185–202.

Wittemann, F., Maertens, R., Kärger, L., Henning, F., 2019. Injection molding simulation of short fiber reinforced thermosets with anisotropic and non-Newtonian flow behavior. Composites Part A: Applied Science and Manufacturing 124, 105476.